SPACOMM 2023

The Fifteenth International Conference on Advances in Satellite and Space Communications

ISBN: 978-1-68558-035-3

April 24th – 28th, 2023

Venice, Italy

SPACOMM 2023 Editors

Timothy Pham, Jet Propulsion Laboratory - California Institute of Technology, USA

SPACOMM 2023

Forward

The Fifteenth International Conference on Advances in Satellite and Space Communications (SPACOMM 2023), held between April 24th and April 28th, 2023, continued a series of events attempting to evaluate the state of the art on academia and industry on the satellite, radar, and antennas-based communications, bringing together scientists and practitioners with challenging issues, achievements, and lessons learnt.

Significant efforts have been allotted to design and deploy global navigation satellite communications systems, Satellite navigation technologies, applications, and services experience still challenges related to signal processing, security, performance, and accuracy. Theories and practices on system-in-package RF design techniques, filters, passive circuits, microwaves, frequency handling, radars, antennas, and radio communications and radio waves propagation have been implemented. Services based on their use are now available, especially those for global positioning and navigation. For example, it is critical to identify the location of targets or the direction of arrival of any signal for civilians or on-purpose applications; smarts antennas and advanced active filters are playing a crucial role. Also, progress has been made for transmission strategies; multiantenna systems can be used to increase the transmission speed without the need for more bandwidth or power. Special techniques and strategies have been developed and implemented in electronic warfare target location systems.

We take here the opportunity to warmly thank all the members of the SPACOMM 2023 technical program committee, as well as all the reviewers. The creation of such a high-quality conference program would not have been possible without their involvement. We also kindly thank all the authors who dedicated much of their time and effort to contribute to SPACOMM 2023. We truly believe that, thanks to all these efforts, the final conference program consisted of top-quality contributions. We also thank the members of the SPACOMM 2023 organizing committee for their help in handling the logistics of this event.

We hope that SPACOMM 2023 was a successful international forum for the exchange of ideas and results between academia and industry and for the promotion of progress in the field of satellite and space communications.

SPACOMM 2023 Chairs

SPACOMM 2023 Steering Committee

Timothy T. Pham, Jet Propulsion Laboratory - California Institute of Technology, USA
Stelios Papaharalabos, u-blox Athens, Greece
Oliver Michler, Technical University Dresden, Germany

SPACOMM 2023 Publicity Chairs

Laura Garcia, Universitat Politecnica de Valencia, Spain
Javier Rocher Morant, Universitat Politecnica de Valencia, Spain

SPACOMM 2023
Committee

SPACOMM 2023 Steering Committee

Timothy T. Pham, Jet Propulsion Laboratory - California Institute of Technology, USA
Stelios Papaharalabos, u-blox Athens, Greece
Oliver Michler, Technical University Dresden, Germany

SPACOMM 2023 Publicity Chairs

Laura Garcia, Universitat Politecnica de Valencia, Spain
Javier Rocher Morant, Universitat Politecnica de Valencia, Spain

SPACOMM 2023 Technical Program Committee

Zahir A. Hussein Alsulaimawi, Oregon State University, USA
Suayb S. Arslan, MEF University, Turkey
Michael Atighetchi, Raytheon BBN Technologies, USA
Peter Baumann, Jacobs University, Germany
Yao-Yi Chiang, University of Southern California - Spatial Sciences Institute, USA
Raed S.M Daraghmah, Palestine Technical University, Palestine
Arun Das, Arizona State University, USA
Yiping Duan, Tsinghua University, China
Nour El Madhoun, Laboratoire Sécurité & Système de l'EPITA (LSE), France
Mohamed A. Elshafey, Military Technical College, Cairo, Egypt
Luiz Carlos Gadelha de Souza, Federal University of ABC, Brazil
Gregory Hellbourg, International Center for Radio Astronomy Research | Curtin University, Western Australia
Sundararaja Sitharama Iyengar, Florida International University, USA
Seifallah Jardak, Bristol Research & Innovation Laboratory - Toshiba, UK
Vladimir Karaev, Institute of Applied Physics of Russian Academy of Sciences, Russia
Baris Kazar, Oracle America Inc., USA
Mohamed Khalaf-Allah, Friedrich-Alexander University of Erlangen-Nuremberg, Germany
Adil Hakeem Khan, Nation College of Engineering and Technology, Guna, India
Arash Komaee, Southern Illinois University, Carbondale, USA
Pablo Madoery, Universidad Nacional de Córdoba, Argentina
Krešimir Malarić, University of Zagreb, Croatia
Michael P. McGuire, Towson University, USA
Oliver Michler, Technical University Dresden, Germany
Sara Migliorini, Università degli Studi di Verona, Italy
Nelli Mosavi, Johns Hopkins University, USA
Nitin Muchhal, Netaji Subhas University of Technology Delhi, India
Tathagata Mukherjee, The University of Alabama in Huntsville, USA
David N. Amanor, Intel Corporation, USA
Brian Niehoefer, TÜV Informationstechnik GmbH, Germany
Nele Noels, Ghent University, Belgium

Copyright Information

For your reference, this is the text governing the copyright release for material published by IARIA.

The copyright release is a transfer of publication rights, which allows IARIA and its partners to drive the dissemination of the published material. This allows IARIA to give articles increased visibility via distribution, inclusion in libraries, and arrangements for submission to indexes.

I, the undersigned, declare that the article is original, and that I represent the authors of this article in the copyright release matters. If this work has been done as work-for-hire, I have obtained all necessary clearances to execute a copyright release. I hereby irrevocably transfer exclusive copyright for this material to IARIA. I give IARIA permission or reproduce the work in any media format such as, but not limited to, print, digital, or electronic. I give IARIA permission to distribute the materials without restriction to any institutions or individuals. I give IARIA permission to submit the work for inclusion in article repositories as IARIA sees fit.

I, the undersigned, declare that to the best of my knowledge, the article is does not contain libelous or otherwise unlawful contents or invading the right of privacy or infringing on a proprietary right.

Following the copyright release, any circulated version of the article must bear the copyright notice and any header and footer information that IARIA applies to the published article.

IARIA grants royalty-free permission to the authors to disseminate the work, under the above provisions, for any academic, commercial, or industrial use. IARIA grants royalty-free permission to any individuals or institutions to make the article available electronically, online, or in print.

IARIA acknowledges that rights to any algorithm, process, procedure, apparatus, or articles of manufacture remain with the authors and their employers.

I, the undersigned, understand that IARIA will not be liable, in contract, tort (including, without limitation, negligence), pre-contract or other representations (other than fraudulent misrepresentations) or otherwise in connection with the publication of my work.

Exception to the above is made for work-for-hire performed while employed by the government. In that case, copyright to the material remains with the said government. The rightful owners (authors and government entity) grant unlimited and unrestricted permission to IARIA, IARIA's contractors, and IARIA's partners to further distribute the work.

Table of Contents

Large-Scale Space Network Simulator for Performance-Optimized DTNs

Nadia Kortas
NASA Glenn Research Center
Cleveland, OH, USA
nadia.kortas@nasa.gov

Timothy Recker
University of California, Berkeley
Berkeley, CA, USA
tjr@berkeley.edu

***Abstract*—High-rate Delay Tolerant Networking (HDTN) is a performance-optimized Delay Tolerant Networking (DTN) implementation that can provide multigigabit per second data rates in disruptive and high-latency space networks. Routing, especially in large-scale space networks, remains challenging due to network topologies that evolve over time. This paper presents a simulation tool that enables HDTN implementation testing at accelerated speeds, which is key for routing in large-scale space networks.**

***Index Terms*—High data-rate Delay Tolerant Networking, performance-optimized space networks, network simulation, DTN routing.**

I. Introduction

Communication in space environments on an interplanetary scale is challenging due to the extreme distances involved, signal propagation delays, and disrupted networks without end-to-end connection. The existing TCP/IP-based internet protocols operate on a principle of providing end-to-end communication and do not tolerate long delays and disruptions. Delay Tolerant Networking (DTN) [1] was designed to address these issues and to operate effectively in such environments achieving reliable automated network communications for space missions by using the bundle protocol which forms a store-and-forward overlay network [2].

With the significant rise in the number of satellites being sent into space, the scale of space communication networks continues to increase, and routing in these space–terrestrial systems remains challenging due to network topologies that evolve over time. At the NASA Glenn Research Center, an implementation of DTN called High-rate Delay Tolerant Networking (HDTN) has been developed with the goal of offering a solution that can scale to large, heterogeneous, interplanetary networks while maximizing performance [3]. However, the typical means for analyzing a network of HDTN nodes is slow and difficult, especially when scaling to large networks or long time periods. Emulations on virtual machines or local laboratory tests on physical machines were time consuming to configure and set up and did not scale to large numbers of nodes. To overcome these challenges, a simulation tool was developed that replicates the routing decisions that HDTN would take in an operative situation but does so in a controllable, easy-to-debug, and accelerated simulation environment. This paper presents (H)DtnSim, a simulator implemented based on DtnSim [4] by extending it to interact with the HDTN routing module. This simulator was created in OMNeT++ [5], a discrete event network simulator platform. DtnSim was built using this event driven framework to simulate scenarios efficiently at accelerated speeds, which is crucial for large-scale space networks where analysis is needed over long duration orbital periods. The structure of this paper is as follows: Section II provides a general HDTN software overview. The simulator design decisions and architecture are described in detail in Section III. Testing results from the tool for four different case studies are presented in Section IV. Section V summarizes the conclusion and simulator enhancements now in development.

II. HDTN architecture

HDTN software, which is available as open-source code [6], was designed with the goal of substantially reducing latency and improving throughput, even in constrained environments. For this reason, it adopts a parallel pipelined and message-oriented modular architecture, allowing the system to scale gracefully as its resources increase. State information is replicated between HDTN modules using ZeroMQ (ZMQ) [7], avoiding the use of shared memory methods of interprocess communication, which were found to create several bottlenecks in similar networking applications [8]. HDTN modules are defined in the following subsections; Figure 1 shows their interactions.

A. Ingress

The Ingress module intakes bundles and decodes the header fields to determine the source and destination of the bundles. If the link is available, Ingress will send the bundles in a cut-through mode straight to Egress; if the link is down or custody transfer is enabled (which involves moving the responsibility for reliable delivery of bundles among different DTN nodes in the network), it sends the bundles to the Storage module. Even if an immediate forwarding opportunity exists, Storage is always required when custody transfer is enabled. The bundle layer must be prepared to retransmit the bundle if it does not receive an acknowledgment within the time-to-acknowledge that the subsequent custodian has received and accepted the bundle.

 ISBN: 978-1-68558-035-3

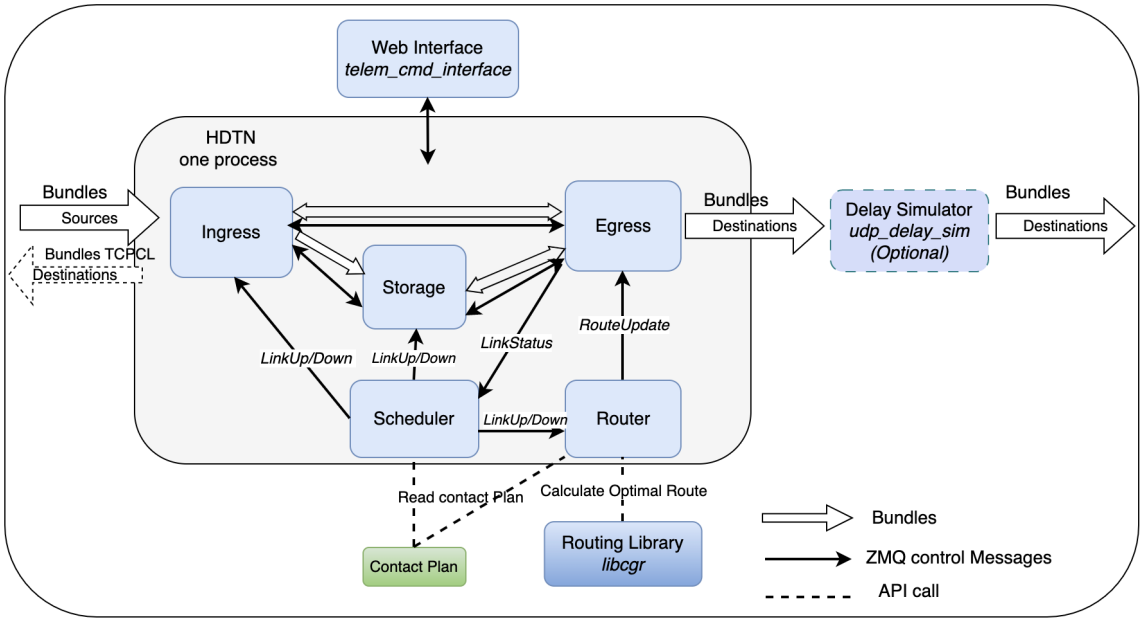

Fig. 1. HDTN software architecture and modules interactions.

B. Scheduler

The Scheduler sends `LinkUp` or `LinkDown` events with time updates to Ingress, Storage and Router. This information is used to determine if a given bundle should be forwarded immediately to Egress or stored, to recompute the route as needed if a link down would invalidate it and to keep updating the Router's own internal time before computing the optimal route. To determine the availability of a given link, the Scheduler reads a contact plan, which is a JavaScript Object Notation (JSON) file that defines all the connections between all the nodes in the network. In addition, the Scheduler dynamically handles unexpected link status changes upon receiving `HDTN_MSGTYPE_LINKSTATUS` from Egress, as well as reloading the entire contact plan upon receiving a `CPM_NEW_CONTACT_PLAN` request.

C. Storage

Storage is a multi-threaded implementation distributed across multiple disks and where custody transfer is handled. It receives messages from the Scheduler to determine when stored bundles can be released and forwarded to Egress.

D. Router

The Router module gets the next hop and best route leading to the final destination using one of the algorithms in the routing library. The router currently supports Contact Graph Routing (CGR), Dijkstra's algorithm (the default algorithm used), and Contact Multigraph Routing (CMR), which is a modified version of Dijkstra's algorithm using a multigraph structure instead of a contact graph and providing a significant performance improvement [9]. The Router then sends a `RouteUpdate` event to Egress to update its outduct to the outduct of that next hop. If the link goes down unexpectedly or the contact plan gets updated, the Router is notified, recalculates the next hop, and sends the `RouteUpdate` event to Egress so that it updates its outduct based on the new next hop.

E. Egress

The Egress module is responsible for forwarding bundles received from Storage or Ingress to the correct outduct and next hop based on the optimal route computed by Router. HDTN uses an event-driven approach based on ZeroMQ pub-sub sockets for sending unexpected link updates and contact plan changes. When the connection changes unexpectedly, Egress will send a `LinkStatus` update message to the Scheduler, which triggers it to send a `LinkDown` or `LinkUp` event to Ingress, Storage and Router to determine whether bundles should be stored or the route needs to be recomputed.

F. Web Interface

The Web Interface displays data rates graph and bundles statistics for network troubleshooting. It's also used for updating configuration, routes, and contact plans.

III. HDTN Simulator Design

Analyzing the behavior of a complete network of HDTN nodes poses some challenges. Unit tests can be used to assess individual modules in HDTN and integrated tests can assess how modules combine to implement HDTN node behavior. However, assessing the behavior of an HDTN network has traditionally required running tests on physical machines or emulations on virtual machines. Laboratory tests of up to

 ISBN: 978-1-68558-035-3

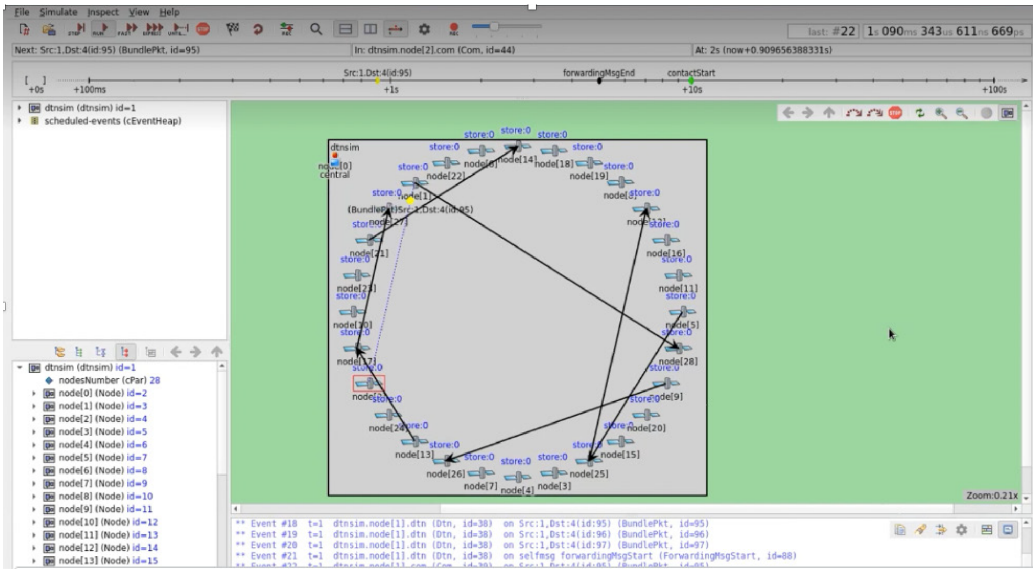

Fig. 2. (H)DtnSim Graphical User Interface (GUI)

ten nodes have been run, but a major design goal of HDTN is to achieve performance and stability that can scale to a large, interplanetary network. Given this goal, existing network analysis methods have two main problems:

- Setting up and configuring tests can be slow. This problem becomes more significant as tests scale to more nodes, contacts, and data transmitted.
- Running tests can be slow. This problem also grows as tests scale to longer time periods.

This section explores simulation as a potential solution to these two testing difficulties. A DTN simulator should exhibit six desirable properties:

(A) **A**ccuracy
(R) **R**un-time acceleration
(U) **U**tility
(D) **D**evelopment-time acceleration
(M) **M**aintainability
(S) **S**calability.

The first three properties are essential for the purpose of HDTN simulation; without them, there would be no reason to simulate HDTN instead of running nodes in the laboratory. Property A means that given the same transmission plan, contact plan, and time-varying network topology, a simulated DTN should produce the same results as a real DTN. R means that simulations should run in an accelerated simulation time instead of real time, i.e., a simulation spanning one hour of the contact plan should take less than one hour of real time to run. U means that the simulator must produce some output that can be processed—either by a machine or a human—and the output should yield some insight about the behavior of the DTN. D and M refer to the man-hour cost of developing simulation scenarios and of maintaining the simulator. S means that as one varies the size of parameters—such as number of nodes, number of contacts, time elapsed, number of bundles sent, and size of bundles sent—all previous properties continue to hold.

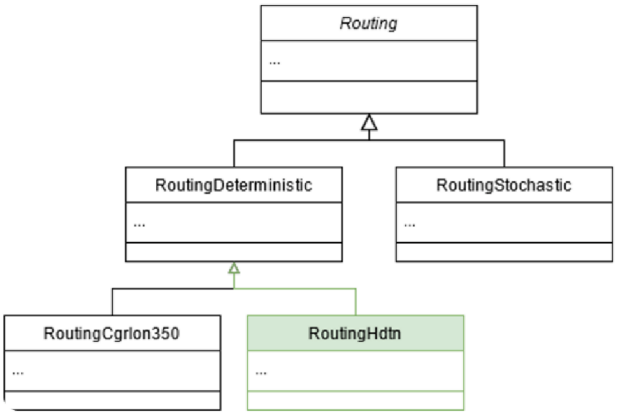

Fig. 3. DtnSim Routing class hierarchy with methods omitted. All Routing models implement the abstract Routing class and RoutingHdtn imitates the RoutingCgrIon350 class.

The approach taken to simulating HDTN in this paper is an extended version of DtnSim, referred to here as (H)DtnSim. DtnSim is a simulator for DTNs with a special emphasis on analyzing routing. It exhibits many of the desirable properties described previously in this section, including accelerated execution in non-real time (R), ease of configuration with short and simple .ini files that can be edited in text mode or using a graphical interface (D), automatic generation of metrics and diagrams for network flows and network topologies (U), and user-friendly interfaces for the visualization and control of simulation scenarios and the analysis and plotting of metrics (U). The (H)DtnSim user-friendly GUI shown in Figure 2 is a key element to gaining insight into complex time-evolving topologies.

 ISBN: 978-1-68558-035-3

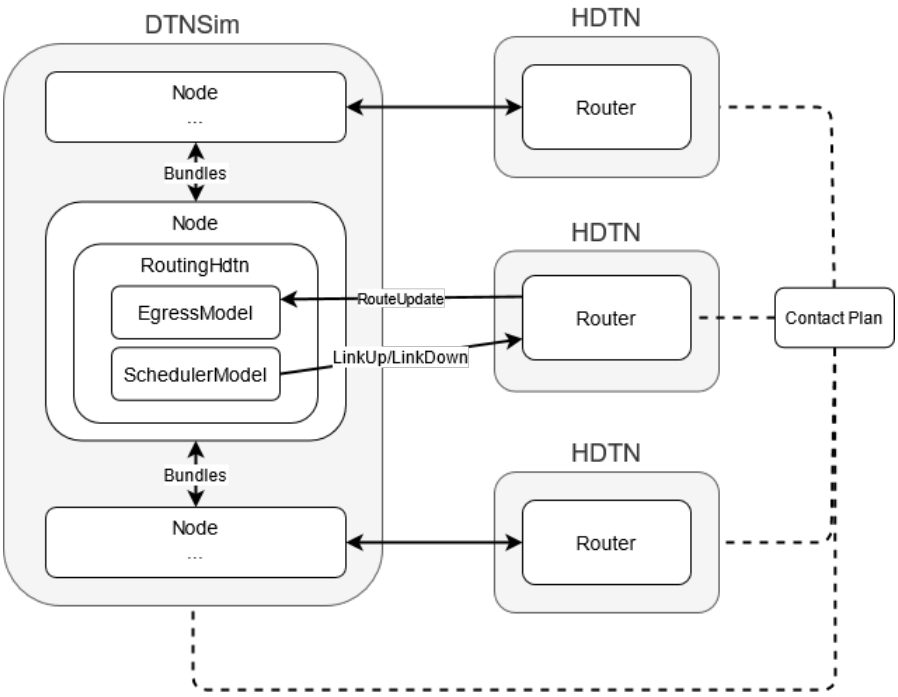

Fig. 4. Illustration of the architecture of (H)DtnSim showing three real HDTN nodes communicating via ZMQ messages with simulated nodes in DtnSim. A shared contact plan must be supplied by the user but HDTN configuration is largely generated by the simulator.

This approach is viable because DtnSim is written in a modular, object-oriented fashion that allows users to select different routing models for their simulations and enables developers to easily implement new routing models as subclasses. It relies on a class hierarchy starting from the `Routing` class and uses virtual methods throughout the code to enable extension through inheritance. Extending the base `Routing` model with subclasses enables a developer to create DTN nodes with custom behavior that can take full advantage of all the features and functionality of DtnSim. Thus, HDTN simulation is achieved by implementing a `RoutingHdtn` class as shown in Figure 3.

Two notable subclasses include `RoutingCgr Model350` and `RoutingCgrIon350`, each of which exhibits distinct and instructive approaches to simulation. The former implements a simplified version of Interplanetary Overlay Network (ION)'s routing logic using the abstractions of DtnSim. The latter can be understood as an interface gluing together DtnSim code and actual ION flight code; ION support in DtnSim is implemented by taking a subset of ION (namely the part that decides when and where bundles are forwarded or stored), compiling it into DtnSim, and calling it from the `RoutingCgrIon350` class. These two classes represent alternative ways to answer the question: "What would ION do?" After determining the answer, they replicate this action in the simulator. The `RoutingCgrIon350` class answers the question by actually running ION in accelerated simulation time and inspecting the result.

Although this approach is clever, its implementation has one notable limitation: copying ION code and compiling it into the simulator requires the simulator to be updated every time ION changes to stay current with ION. This has left ION support in DtnSim frozen at ION version 3.5.0, even though the latest version is 4.1.1. This Maintainability limitation is too costly for an HDTN simulator to embrace, given that HDTN—especially the functionality of the Router—is under active research and development. Over the ten weeks during which the research for this paper was conducted, HDTN was enhanced with several additions, including a CGR library written in C++, an implementation of the CMR algorithm, and features for time-tracking and route re-computation. Additionally, during this time, developers were researching a routing approach based on Spiking Neural Networks (SNN) using estimations and observations of the network congestion and loss, neighbor discovery and other routing enhancements.

Considering these maintainability concerns, (H)DtnSim takes the same general approach as `RoutingCgrIon350` while addressing the Maintainability issue by applying classical principles of engineering and object-oriented software: information hiding and restricting interaction between entities to limited public interfaces. HDTN itself is written in a modular, object-oriented fashion since it consists of five modules interacting through asynchronous message passing. Thus, instead of embedding HDTN within DtnSim, the authors chose to extend DtnSim with the ability to talk to HDTN: an HDTN Router process runs for each DtnSim node, communicating using the messaging protocol of HDTN over ZMQ sockets, as shown in Figure 4. Here are the steps for per-node Router initialization:

1. Map the EID of the node to a pair of unique port numbers.

 ISBN: 978-1-68558-035-3

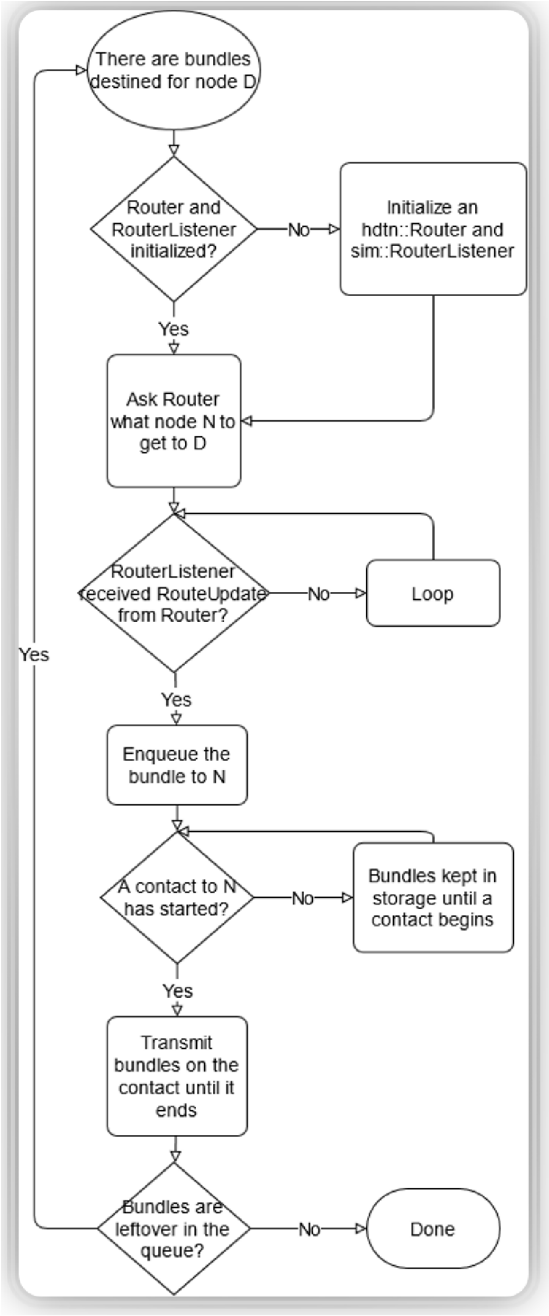

Fig. 5. Flow diagram of steps HdtnRouting takes to decide where bundles go.

2. Generate an HDTN configuration file that binds the Scheduler and Router to the generated port numbers on the localhost.
3. Run an hdtn-router executable installed on the user's system using the configuration file generated in the previous step.
4. Connect objects of types SchedulerModel and EgressModel to the Router.

The flow diagram in Figure 5 shows the steps HdtnRouting takes to decide where bundles go. The SchedulerModel sends `LinkUp`/`LinkDown` messages to the Router to keep the Router's internal notion of time synchronized with the simulator and notify it of relevant network topology changes. The EgressModel listens for `RouteUpdate` messages published by the Router and uses the Router's decision to replicate the equivalent action in DtnSim. Combined with the event loop of DtnSim facilitated by OMNeT++ messages, the SchedulerModel models the required functionality of an HDTN Scheduler module; combined with the bundle forwarding threads and the event loop, the EgressModel models the functionality of an HDTN Egress module. In other words, these two models are simplified versions of HDTN modules that stand in for the actual modules and mimic their behavior.

IV. Testing and Results

In this section, a series of simulation scenarios illustrates how this implementation exhibits the six properties desired, making it a simulator suitable for analyzing HDTN.

A. Simulator vs Runscript

To test the accuracy of the simulator, two routing test cases from the HDTN source code have been mimicked in a simulation scenario. The first is copied from a shell run script and involves one node sending bundles to two other nodes. The second is the "routing test" contained in the Linux scripts directory of the HDTN source code and involves four nodes in a network where Node 1 sends bundles to Node 4. Both tests use the same contact plans used by the HDTN test cases and produce approximately the same outcomes as summarized in Table I. For both the runscript and simulator the actual number of bundles delivered is approximately as expected and matching but there is a 1% discrepancy. In the simulator precisely 3800 bundles are delivered while in the runscript anywhere from 3834-3840 bundles are delivered with some indeterminacy. The cause of this is under investigation but there are a couple possible explanations. First, it may be that there is some imprecision in the bundle generator used in the runscript such that it does not produce exactly 100 bundles per second. Second, it may be that because the bundle generator and HDTN's Scheduler don't share a clock there is some asynchronization such that the bundle generator produces 37-40 bundles before the Scheduler is fully running and tracking time. In contrast, in DtnSim both the application layer and the underlying DTN layer share a single notion of time and are tightly synchronized. DtnSim supports the use of random variation in parameters that could allow more accurate description of the real HDTN scenario within the simulator with some additional effort. However, both of these potential effects might be heavily system dependant and difficult to quantify. Despite these nuances, this test demonstrates that A holds within a small margin of error.

Additionally, the results for the run script test detailed in Table I show that the simulation versions of the tests have a lower development time and run time. The run time can easily be measured with a physical or software stopwatch. Development time is difficult to measure precisely but as a proxy one can look at the total number of Source Lines Of Code (SLOC) that must be written to implement a scenario.

 ISBN: 978-1-68558-035-3

TABLE I
COMPARISON OF SIMULATION AND RUNSCRIPT PERFORMANCE

	Simulation	Runscript
Routes Found	$10 \rightarrow 2$, $10 \rightarrow 1$	$10 \rightarrow 2$, $10 \rightarrow 1$
Actual Bundles delivered	3800	3840 ± 6
Config lines (SLOC)	13	158
Run time (s)	1	73 ± 3
Discrete events	34558	NA

B. CGR vs CMR

As stated in Section III, a major design goal of the simulator is to abstract internal implementation details of HDTN so that HDTN can continue to develop without requiring updates to the simulator. This goal was put to the test by running two different branches of the HDTN source code in the simulator. The first branch used a CGR version of Dijkstra's algorithm to compute the best routes; the second used a CMR algorithm. These algorithms have different definitions, run-time complexities, and implementations, yet the simulator worked equally well with either branch. HDTN implementations can be swapped easily within the simulator, requiring no changes to simulator source code and only a one-line configuration file change. Thus, M holds. (H)DtnSim can deliver this flexibility and Maintainability under two conditions: 1. The architecture of HDTN cannot change, including changes to the structure or semantics of the messages passed between HDTN modules 2. The user interface to HDTN must remain backwards compatible, i.e., the command line interface must continue to support the syntax and options that the simulator uses to run HDTN.

If either of these conditions is unmet, the simulator might require updates to continue working with the latest version of HDTN. Architectural and interface updates amount to changing the design of HDTN. Given that the simulator models the behavior of HDTN, it is hardly surprising that such design changes necessitate updates to the simulator that models it. However, as long as the design of HDTN remains stable, changes in implementation details will not negate the accuracy of the simulator's model. This approach comes with a few noteworthy requirements or limitations:
1. (H)DtnSim must implement some of the messages that HDTN uses.
2. (H)DtnSim must use only these messages to get information about the running HDTN Router; dissecting the internal state of the Router compromises the abstraction layer.
3. (H)DtnSim must interpret the semantics of these messages in a way that is equal to the HDTN interpretation or at least similar enough to replicate HDTN's behavior.

Because of the flexible nature of (H)DtnSim, performance enhancements can be made to HDTN without requiring a change to the simulator. Thus, in addition to facilitating Maintainability, this property of the simulator supports HDTN's core performance mission.

C. HDTN vs ION

The simulator has been used to identify useful enhancements to HDTN by running simulation scenarios for both HDTN and ION and comparing the results. As the flow diagrams in Figures 6 and 7 indicate, ION can transmit 1,728,000 bytes over the last contact in the simulation for a total of 7,680,000 bytes transmitted; in HDTN, those bytes remain stranded on node one, resulting in a bundle loss rate of 22.5 percent. After inspecting the HDTN source code, it was determined that this difference in packet delivery rate was primarily the result of the way the HDTN Router handled time and changes in the network topology. In particular, the Router formerly did not update its time from the initial time of the contact plan, nor did it recompute routes when a link down event should make a route it previously computed invalid.

The effect of this problem is difficult to quantify generally because it heavily depends on the precise contact graph and network traffic. Thus, the difference in bundle delivery rates between ION and HDTN resulting from this issue could be 0%, 100%, or anything in between. However, bundle delivery rate is an important performance metric and the situation that produced this discrepancy between ION and HDTN is quite plausible in realistic network topologies and workloads; all it requires is that the Router computes a route for some bundles and one of the links in this route later goes down while previously routed bundles are still awaiting delivery. The discovery of this problem and the clarity of its illustration is a strong testament to the Utility of (H)DtnSim.

As a result of this discovery, enhancements to HDTN time-tracking and route computation were made, resulting in the changes illustrated in the network flow diagrams of Figures 8 and 9. These enhancements were implemented with architectural changes to HDTN, which required updates to the simulator that are under development. This is a good example of the limits of property M: the simulator is resilient to internal implementation changes but can require significant updates when changes are made to HDTN's ZMQ sockets, message structure, message semantics or CLI options.

D. Scaling to Large Networks

For this section, the simulations were constructed with four fictitious ground stations, at Albany, NASA Glenn Research Center, University of California Berkeley, and Guam based on data from Starlink satellite orbits. With each simulation lasting for 24 hours (86400 seconds), and counting the ground stations as nodes, the contact plans consisted of 14, 54, 104, and 204 nodes corresponding to 368, 7186, 28162, and 109330 contacts, respectively.

TABLE II
SIMULATION RESULTS USING THE FOUR LARGE CONTACT PLANS

Nodes	14	54	104	203
Contacts	368	7186	28162	109329
Time (s)	5	7	15	94
Discrete events	611460	2157761	3098460	6658661

 ISBN: 978-1-68558-035-3

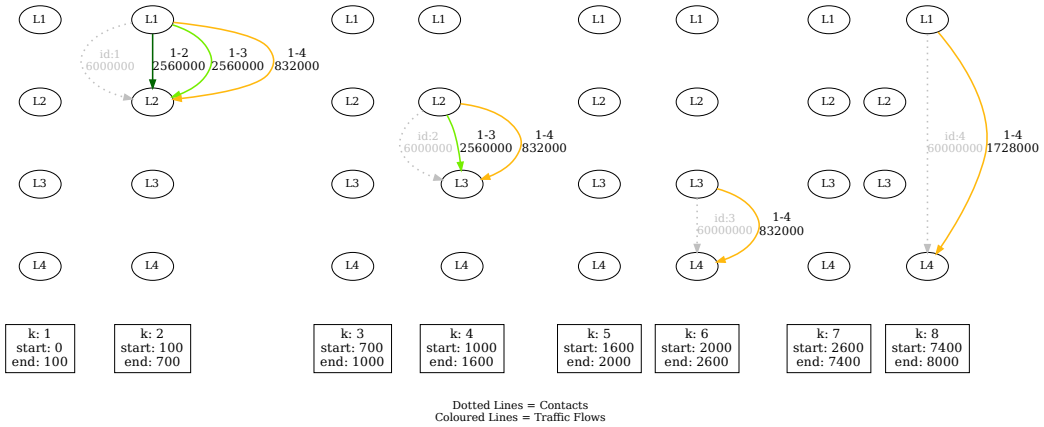

Fig. 6. A data flow diagram for a network of four nodes running ION. All links are utilized in this scenario for 100% bundle delivery rate.

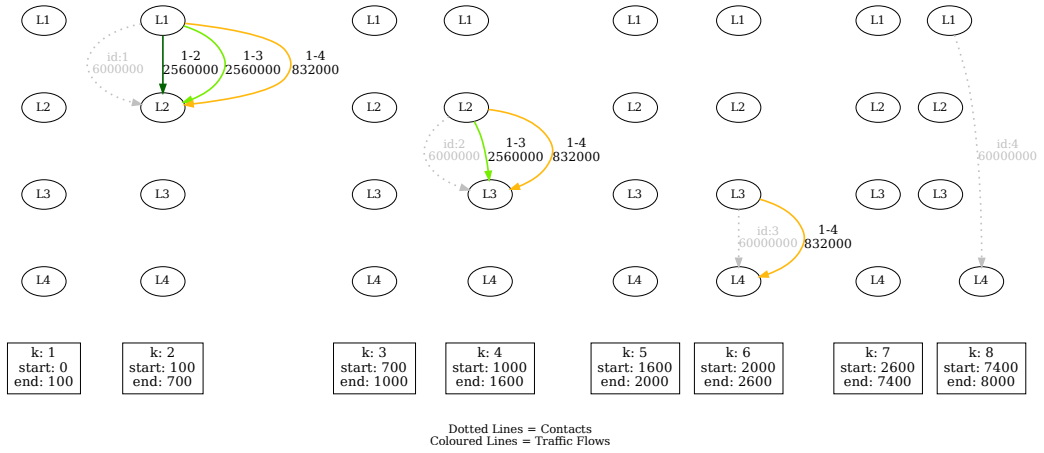

Fig. 7. A data flow diagram showing how HDTN handled the same scenario shown in Figure 6. The link from L1 to L4 in the last network topology is not utilized, resulting in bundle loss.

The data in Table II and Figures 10 and 11 show the results of a simple, fixed scenario run with the four contact plans described. The network is populated by nodes connected through intermittently connected, gigabit-rate links. For 20 seconds of simulation time, one ground station sends 1907 bundles per second consisting of 65535 bytes to another ground station, using routes with two hops via satellite. These values are selected to saturate the gigabit links with bundles equal in size to the maximum size of a TCP packet. In each of the four runs, this situation is constant and only the number of nodes and contacts varies.

These results—combined with preliminary inspection of the effects of bundle count and route recomputation—suggest that the duration of a simulation depends on (a) the number of discrete events in the simulator and (b) the time spent running the HDTN Router. The former is mostly—aside from a small extra startup overhead—independent of the number of nodes, length of simulated time, and size of bundles sent; it depends instead on the number of contacts and number of bundles sent. However, in a dense network topology (graph) the number of contacts (edges) will increase quite rapidly with the number of nodes (vertices). Thus, the results of x, y, z show a steep jump in simulation runtime in the step from 104 to 203 nodes since the topologies in this scenario are somewhat dense. This issue should look familiar to readers aware of the challenges resulting from the amount of scheduling information required to use CGR in large networks. However, a sparse network topology would not face this issue.

On the other hand, part of the time spent running the HDTN Router depends on the implementation and computational complexity of HDTN's routing algorithm. This part indicates nothing about the performance of the simulator itself. However, time spent running the HDTN Router also depends on the simulator implementation. Some performance optimizations

 ISBN: 978-1-68558-035-3

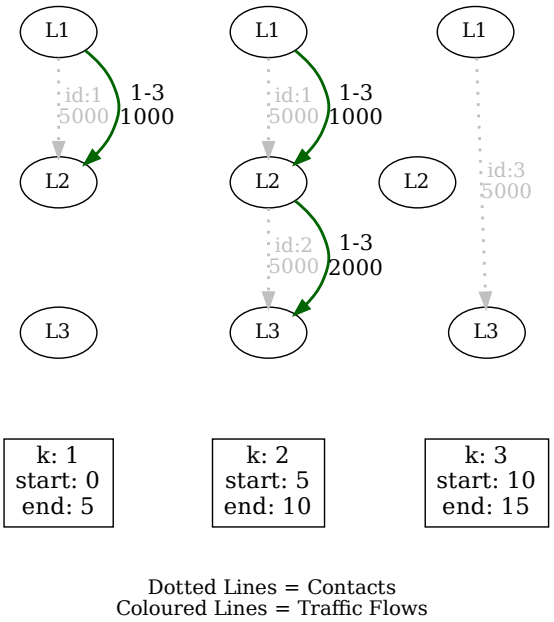

Fig. 8. Data flow diagram before Router changes. A link from L1 to L3 is available in the third network topology but is not utilized to transmit bundles because the Router did not track time and thinks the next hop should still be L2.

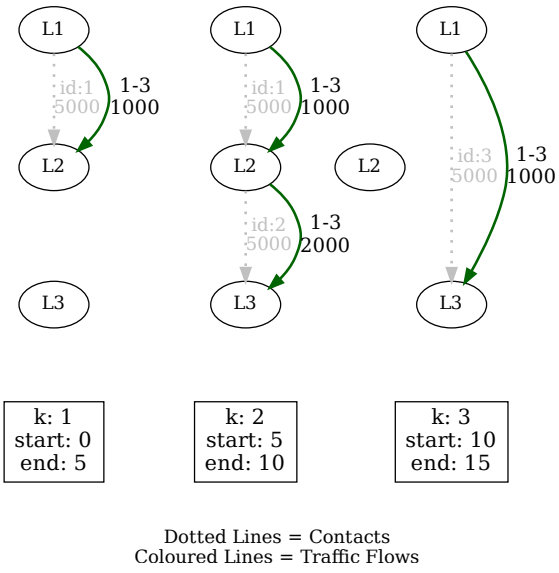

Fig. 9. Data flow diagram after Router was updated to track time. Unlike in Figure 8, the link from L1 to L3 is properly utilized to deliver bundles.

have been implemented to address this, such as caching results from the HDTN Router. Others, like more efficient

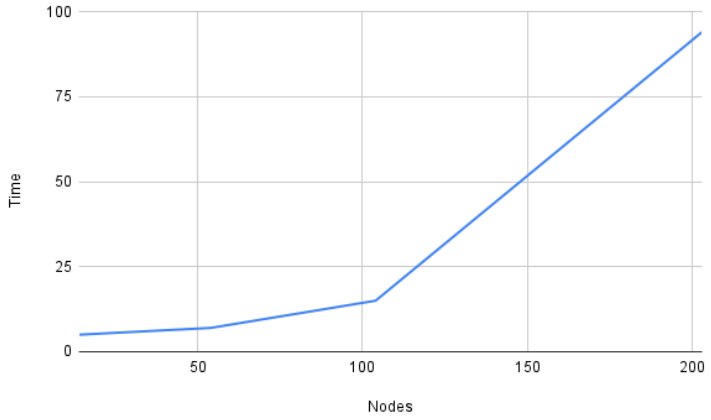

Fig. 10. The most significant factor in simulator performance when scaling to large networks is the time (in seconds) required to run a simulation versus node count.

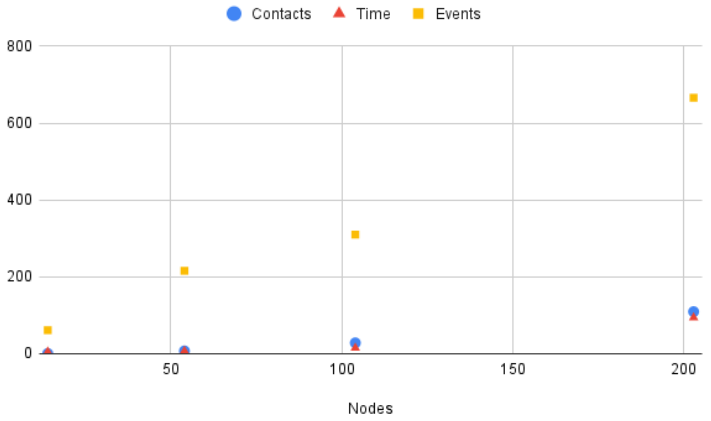

Fig. 11. Contacts expressed in thousands, time in seconds, and events in tens of thousands. Scaled to fit on one plot to show the corresponding slopes.

use of Linux threads and processes, are under development. The simulations in this section are run in a VirtualBox VM on a commodity laptop with no setup tuning. As such, the numbers indicate little about expected runtimes for simulations running with plentiful resources. They do, however, give some idea of how performance persists or degrades with larger networks. The results suggest that (H)DtnSim is successful in *S*caling to networks with many nodes. While simulation performance could be improved, it may be limited by the inherent complexity of the algorithms and the rate of growth for contacts when nodes are added.

V. Conclusion and Future Work

From this research, one can see that a simulator—and the (H)DtnSim simulator in particular—is a satisfactory solution to some problems with testing in HDTN. In addition to the expected and intended outcomes, the simulator facilitates exploration and discovery of HDTN behavior through rapid development and deployment of tests. This process

 ISBN: 978-1-68558-035-3

produced enhancements to the HDTN Router's handling of time, improving bundles delivery rate. The design of HDTN has proven highly modular, flexible, and extensible, making enhancements like these easy to incorporate and interaction with the simulator seamless and maintainable.

(H)DtnSim has been made available publicly to the DTN community under the branch "support-hdtn" [11], which can be found in the official DtnSim repository [4].

Future versions of (H)DtnSim will support the multi-destination routing enhancements. It will also support opportunistic links and unexpected link disruptions. Doing more extensive testing by running simulations on more powerful servers will strengthen the evidence for the claims made about the simulator and provide more insights about HDTN performance.

ACKNOWLEDGMENT

The authors would like to thank the NASA Space Communications and Navigation (SCaN) program. Support from the rest of the HDTN team and guidance from the DtnSim developers, including Juan Fraire and Pablo Madoery, is much appreciated.

REFERENCES

[1] V. Cerf et al., "Delay-Tolerant Networking Architecture," RFC 4838, IETF: Fremont, CA, USA, 2007. [Online]. Available: https://datatracker.ietf.org/doc/rfc4838/. Accessed March 24, 2023.

[2] K. Scott and S Burleigh, "Bundle Protocol Specification," RFC 5050, IETF Network Working Group (2007. [Online]. Available: https://www.rfc-editor.org/rfc/rfc5050. Accessed March 24, 2023.

[3] A. Hylton et al., "New Horizons for a Practical and Performance-Optimized Solar System Internet," IEEE Aerospace Conference, 2022. [Online]. Available: https://doi.org/10.1109/AERO53065.2022.9843598. Accessed March 24. 2023.

[4] J. Fraire and P. Madoery. (2019). DtnSim Official Repository. [Online]. Available: https://bitbucket.org/lcd-unc-ar/dtnsim/src/master/. Accessed March 24, 2023.

[5] A. Varga. "The OMNeT++ Discrete event simulation system," in Proc. European Simulation Multiconference, Prague, Czech Republic, 2001, pp.1-7.

[6] B. Tomko, N. Kortas, R. Dudukovich, and B. LaFuente. (2021). HDTN Official Repository. [Online]. Available: https://github.com/nasa/HDTN. Accessed March 24, 2023.

[7] P. Hintjens. (2020). ZeroMQ: Messaging for Many Applications [Online]. Available: https://zeromq.org/. Accessed March 24, 2023.

[8] A. Hylton, D. Raible, and G. Clark, "On the Development and Application of High Data Rate Architecture (HiDRA) in Future Space Networks," AIAA 2017-5415. [Online]. Available: https://arc.aiaa.org/doi/pdf/10.2514/6.2017-5415. Accessed March 24, 2023.

[9] R. Kassouf, "Contact Multigraph Routing: Overview and Implementation," presented at the 2023 IEEE Aerospace Conference, Big Sky, MT, March 4-11, 2023, Paper 4.0906.

[10] T. Recker. (2022). HDTN Example Simulation [Online]. Available: https://bitbucket.org/lcd-unc-ar/dtnsim/src/master/. Accessed March 24, 2023.

[11] T. Recker. (2022). (H)DtnSim Branch. [Online]. Available: https://bitbucket.org/lcd-unc-ar/dtnsim/src/support-hdtn/. Accessed March 24, 2023.

 ISBN: 978-1-68558-035-3

Characteristics and Performance of Algerian Satellite Based Augmentation System (AL-SBAS)

Lahouaria Tabti
Department of Space Geodesy, Centre of Space Techniques,
Algerian Space Agency
Email: ltabti@cts.asal.dz

Salem Kahlouche
Department of Space Geodesy, Centre of Space Techniques,
Algerian Space Agency
Email: skahlouche@cts.asal.dz

Abstract— The Algerian Satellite Based Augmentation System (AL-SBAS) is developed by the Algerian Space Agency (ASAL) and is based on Algerian geostationary satellite Alcomsat-1. AL-SBAS permits to transmit SBAS messages according to the international standards defined by the International Civil Aviation Organization (ICAO). Compared to existing SBAS, currently the service area of AL-SBAS is limited to Algeria only. Thus, the number of Ionospheric Grid Points (IGP) and satellites "to be increased " is lower than the existing SBAS, in particular the European Geostationary Navigation Overlay Service (EGNOS). The Al-SBAS correction messages are calculated by the Data-Processing Center (DPC) using GPS satellite data collected from a terrestrial network of 18 Reference Stations (RS), which are geographically distributed over the entire country. This work presents the main characteristics and preliminary performance tests of the AL-SBAS System. The analysis concerns in particular the parameters of pseudo-range and ionospheric correction, as well as the integrity transmitted by the system. Very promising results have been achieved considering the number of currently available reference stations in the south of Algeria, which is a region EGNOS does not cover. The ionospheric indicators using EGNOS are between 8 and 15, while the AL-SBAS allows to have indicators ranging between 6 and 13.

Keywords-GPS; AL-SBAS; EGNOS; Indicators of Precision; Integrity.

I. INTRODUCTION

A Satellite Based Augmentation System (SBAS) is an augmentation system that transmits the complementary information to correct errors of measurements and to ensure integrity. SBAS broadcasts corrections of the Global Navigation Satellite System (GNSS) satellite clock, satellite orbital error and corrections of ionospheric delays related to the signal propagation to improve positioning performance [1].

Many countries have established their own SBAS's. Currently, there are four operational SBAS, including the US Wide Area Augmentation System (WAAS), the European EGNOS system, the Indian GPS Aided Geostationary Augmented Navigation (GAGAN), and the Japanese Multi-functional Satellite Augmentation System (MSAS). Russia has also deployed its SBAS system, named the System for Differential Corrections and Monitoring (SDCM). In addition, some countries, such as Australia, Nigeria, and Korea, are testing their SBASs named the Southern Positioning Augmentation Network (SPAN), Nigerian Satellite Augmentation System (NSAS) and Korea Augmentation Satellite System (KASS) respectively**.** China is planning to broadcast SBAS messages via BeiDou Satellite-Based Augmentation System (BDSBAS) [2] [3].

Algeria is also one of the countries that is implementing a similar augmentation system based on the geostationary satellite Alcomsat-1, in order to provide services for Algeria and the surrounding area.

Alcomsat-1 communications satellite was launched on December 11, 2017, and is located at 24.8° W in a geostationary orbit. Figure 1 illustrates the coverage of Alcomsat-1 Navigation Overlay Services named AL-SBAS. The coverage of Alcomsat-1 includes the entire Africa, South America and part of Europe. Alcomsat-1 Communications Satellite is equipped with 33 transponders, including L1&L5 signals navigation augmentation (the other bands are Ku and Ka) [4]**.**

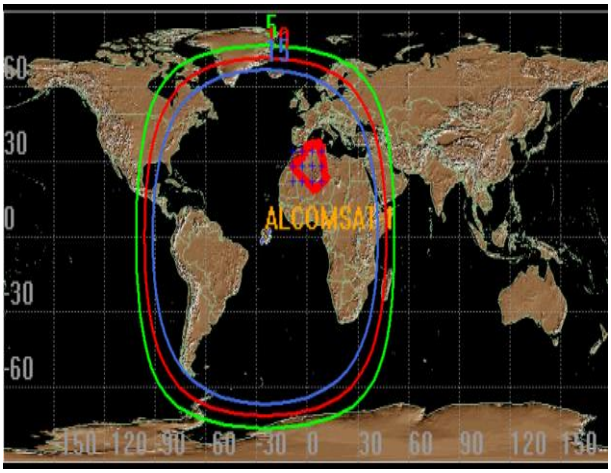

Figure 1. Coverage of Alcomsat-1 Navigation Overlay Services.

The AL-SBAS permits to improve the positioning accuracy and integrity in Algeria and the nearby countries. The system aims to provide SBAS services not only for aviation users but also for other general users, such as surveying, transportation and railways, etc.

The AL-SBAS collects GPS observations and corrects GPS satellites ephemeris errors, clock errors, and ionospheric errors together with the corresponding integrity parameters in real-time. The system broadcasts differential corrections through geostationary satellite (Alcomsat-1) with a high accuracy and a significant capability for integrity augmentation.

 ISBN: 978-1-68558-035-3

The mathematical model of the corrected observation equation using AL-SBAS messages is defined as follows [5]:

$$l_{corr} = l_{mes} + RC_{fast} + RC_{clock} - RC_{iono} + RC_{tropo} \quad (1)$$

where l_{corr} is the pseudo - range for position determination application, l_{mes} is the measured pseudo - range, RC_{fast} is the fast corrections, RC_{clock} is the clock corrections, RC_{iono} is the ionospheric corrections and RC_{tropo} is the tropospheric corrections.

The main objectives of this work consists of analysing the evaluation of AL-SBAS corrections in Algeria and comparing the results with EGNOS.

The rest of the paper is structured as follows. Section II presents the Algerian augmentation system. Section III shows the results of the study. We conclude our work in Section IV.

II. OVERVIEW OF THE ALGERIAN AUGMENTATION SYSTEM (AL-SBAS) BASED ON ALCOMSAT-1

The AL-SBAS system functionality is similar to the SBAS, where a number of ground reference stations monitor the GPS satellites signals and provide their observations to one or more Master Control stations. An augmentation message is generated and transmitted via uplink stations within the uplink the coverage area of the geostationary satellite. Finally, this satellite broadcasts these signals regionally to users with messages to improve positioning accuracy and integrity.

AL-SBAS consists of 18 RS that are installed only in Algeria and are covering all the Algerian territory, one DPC and one Ground Uplink Land Station in Algiers (GULS) [6].

A summary description of the AL-SBAS architecture is provided in Figure 2.

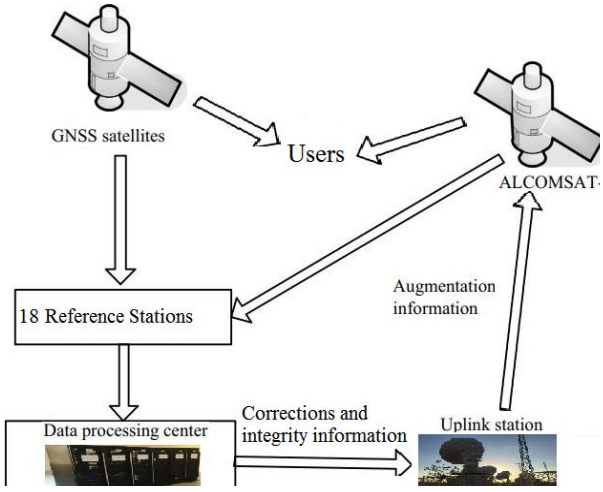

Figure 2. AL-SBAS system description.

A. Overview of AL-SBAS L1 Signal

The structure of AL-SBAS signal is defined to have full compatibility with the SBAS signal. The generator of Pseudo-Random Noise (PRN) code for spreading spectrum is the same as GPS/SBAS L1 (1575.42 MHz).

The following PRN code number 148 is allocated to AL-SBAS for use on L1 C/A code; Table 1 presents the PRN assignments for the AL-SBAS system published in October 2021 [7].

TABLE 1. PRN ASSIGNMENT TO AL-SBAS FOR USE ON L1 C/A CODE

PRN Code Number	PRN Allocations	Orbital Slot
148	ASAL (Alcomsat-1)	24.8 W

The AL-SBAS message structure is like other SBAS composed of 8-bit preamble (to ensure the synchronization of frame), 6-bit to define the Message Type (MT), 212-bit data field to provide corresponding data, and 24-bit Cyclic Redundancy Check (CRC) parity. Figure 3 illustrates all the correction parameters and integrity information that are included in 250-bit data every second [8].

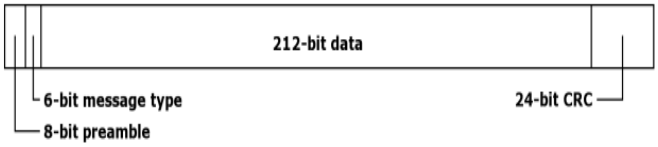

Figure 3. AL-SBAS message structure.

B. Overview of AL-SBAS L1 Correction

AL-SBAS transmits messages in hexadecimal format; an example of the AL-SBAS raw message is given by Figure 4 on 1 December, from 1:00:01 to 1:00:10 with message type MT: 0, 2, 3, 4, 0, 25, 0, 2, 3 and 4.

```
148 22 12 01 00 00 01 0 5302000000000000000003FC4000003FC000000003BBBBBBA797BBB7E30DC0
148 22 12 01 00 00 02 2 9A080000000000000000003FC4000003FC000000003BBBBBBAB97BBA939C300
148 22 12 01 00 00 03 3 C60E0003FD3FD4003FE4000003FC8003FDC000003FDBB97B3BAF9FB9B57D65C0
148 22 12 01 00 00 04 4 53113FD0000000000000000000000000000000000000017BBBBB8000000165F9140
148 22 12 01 00 00 05 0 9A000000000000000000003FC4000003FC000000003BBBBBBAB97BBA4C03A00
148 22 12 01 00 00 06 25 C6664098068010000000000000000000094AC01FFE7F1000000000000027B04180
148 22 12 01 00 00 07 0 5302000000000000000003FC4000003FC000000003BBBBBBAB97BBBAB905C0
148 22 12 01 00 00 08 2 9A080000000000000000003FC4000003FC000000003BBBBBBBBBBBB9EAA01C0
148 22 12 01 00 00 09 3 C60E0003FD3FD4003FE4000003FC8003FDC000003FDBBBBBBBBBBBBA1CC20C0
148 22 12 01 00 00 10 4 53113FD0000000000000000000000000000000000000003BBBBBBB8000013C31280
```

Figure 4. AL-SBAS raw message on December 1, 2022.

AL-SBAS generates three types of differential corrections that are summarized in Table 2.

TABLE 2. DIFFERENTIAL CORRECTION MESSAGES FOR AL-SBAS

MT	Data Type
1	PRN Mask
2-5	Fast correction
24	Mixed fast/long-term satellite correction
25	Long-term satellite error corrections
18	Ionospheric grid point masks
26	Ionospheric delay corrections

In addition to differential corrections, the SBAS also monitors and broadcasts the integrity of GPS satellite signals. The user can determine which satellites and IGP are usable for reliable positioning computation.

C. AL-SBAS Transmission Test

The test transmission of AL-SBAS with code PRN 148 on Alcomsat-1 geostationary satellite was started in July 20, 2020. Currently, this system is intended for test and development purposes only, which will be refined and developed to become a fully certified and operational SBAS for the Algerian region.

The AL-SBAS transmission was not permanently available for each day of year 2021 and during daytime until 21 May (DOY 142). To observe the function of the AL-SBAS in 2021, an analysis of transmitted messages has been performed for that year. These messages are available on the CNES Navigation and Time Monitoring FTP Service [9]. It gives access to AL-SBAS, which allows in an easier way to find and download files, which allows in an easier way to find and download files, regarding the AL-SBAS historical data. Figure 5 shows the number of messages transmitted by AL-SBAS for each day of the year 2021.

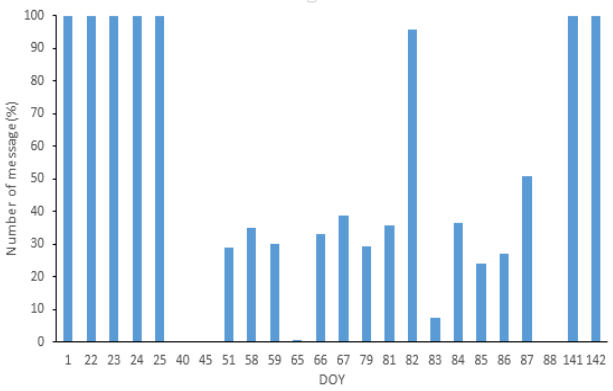

Figure 5. Histogram of Availability and the number of messages transmitted by AL-SBAS during year 2021. The Histogram is based on data from CNES site [9]. The days where no message is transmitted are not presented.

For 2021, there were days and times in which the system did not send any messages. The AL-SBAS satellite broadcasts one message per second and thus the number of SBAS messages during a period of 24 hours is 86400 (100%).

The total message count for AL-SBAS messages varies for each day of the year and (from) hour-to-hour. In particular, the total message count for day 22, 23, 24, 25, 82, 141 and 142 was close to 100%.

III. PURPOSE AND STUDY RESULTS

The main purpose of this work is to test the current AL-SBAS performance and compare these results with EGNOS in Algeria without Ranging and Integrity Monitoring Stations (RIMS).

The corrections of AL-SBAS and EGNOS are downloaded from the CNES FTP server [9]. These files are provided in the RINEX - B format [10]. The analysis was performed for the time period December 1st to 6th, 2022.

A. Analysis Result of Satellite Status

The augmented information related to satellite orbital and clock errors is calculated using MT 1, 2 to 5, 24 and 25. MT 1 provides a Pseudo Random Noise (PRN) mask that specifies the PRN number of the augmented satellite. MT 2 to 5 and 24 provide fast corrections and User Differential Range Error Indicators (UDREI). The UDREI values range from 0 to 15. UDREI equal to 14 means that the satellite is not monitored, while if it is equal to 15 means that it is not used [11], MT 24 and 25 provide long-term correction. Histograms of UDREI parameters for 32 GPS satellites using EGNOS are presented in Figure 6.

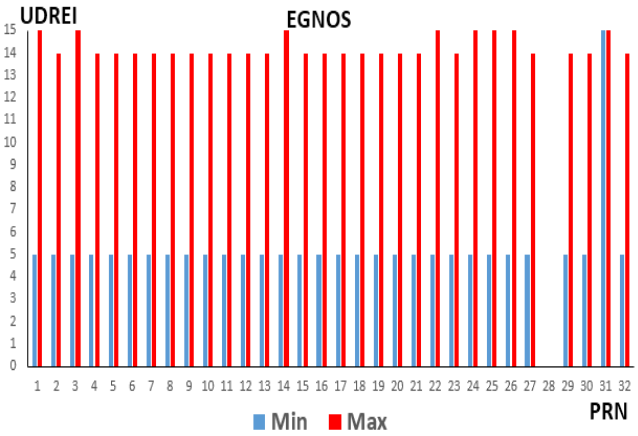

Figure 6. UDREI indicators of each satellite GPS using EGNOS.

By analyzing the indicators of precision transmitted by EGNOS, we notice that these indicators vary between 5 and 15, which means there are some satellites that are not monitored by the system and that the system recommends not to use some satellites. On the other hand, the indicators transmitted by AL-SBAS vary between 5 and 14, as shown in the histogram of the Figure 7.

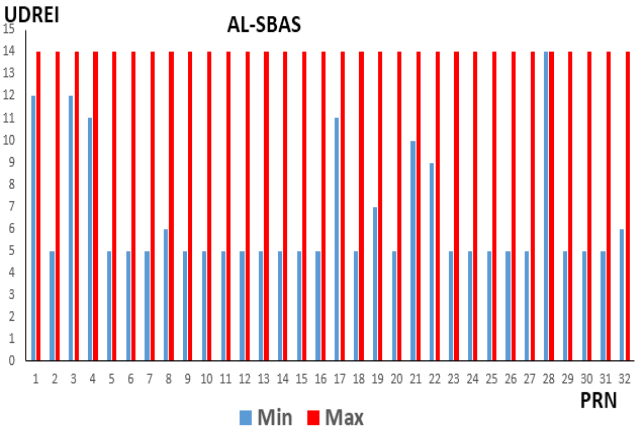

Figure 7. *UDRE* indicators of each satellite GPS using AL-SBAS.

 ISBN: 978-1-68558-035-3

B. Analysis Result of Ionospheric Error

The ionospheric correction is calculated using the information from MT 18 and 26. MT 18 provides the IGP mask that indicates the position of IGP and MT 26 provides ionospheric correction GIVD (Grid Ionospheric Vertical Delay) and indicators GIVEI (Grid Ionospheric Vertical Error Indicator) for each IGP. The GIVEI values range from 0 to 15. GIVEI equal to 14 means that the status of the IGP is not monitored, while if it is equal to 15 means that it is not usable [12].

The analysis result of MT 18 and 26, which are related to the ionospheric error correction shows that the AL-SBAS and EGNOS broadcast ionospheric corrections in the area [-25, +25] degree in longitude and [+5 ,+50] degrees in latitude and [-80, +80] degrees in longitude and [+10,+85] degrees in latitude, respectively. Figures 8 and 9 present the IGPs covered by AL-SBAS and EGNOS transmissions.

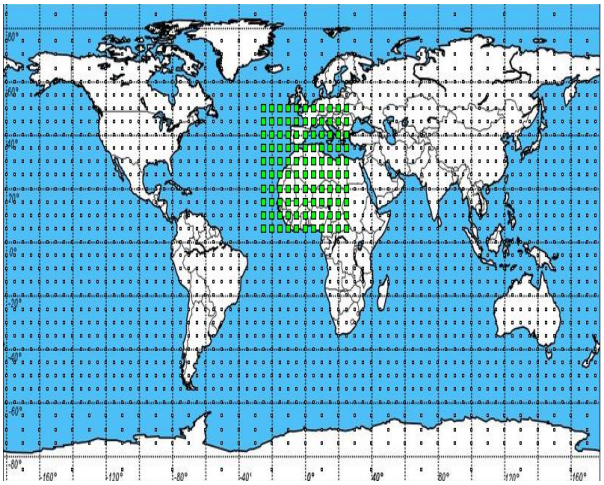

Figure 8. IGPs covered in AL-SBAS transmissions.

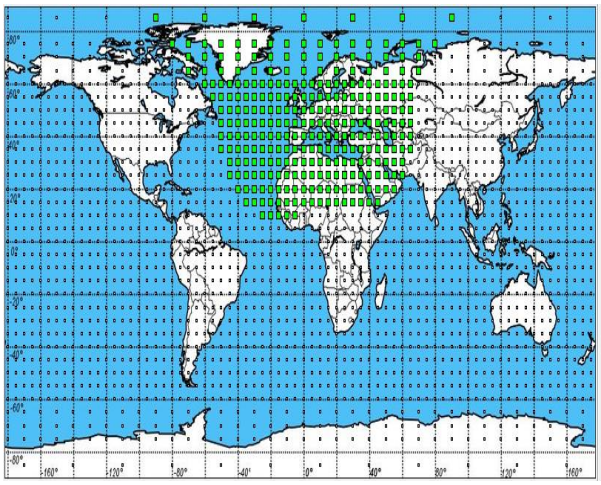

Figure 9. IGPs covered in EGNOS transmissions.

The vertical delay and indicators transmitted by AL-SBAS and EGNOS for two IGP of Lat 35 N, 25 N and long 0 E are given in Table 3.

TABLE 3. VERTICAL DELAY AND GIVDI TRANSMITTED BY AL-SBAS AND EGNOS FOR 2 IGP (LAT 35 N, 25 N AND LONG 0 E)

	AL-SBAS		EGNOS	
	Lat 35 N	Lat 25 N	Lat 35 N	Lat 25 N
GIVD(m)	2.22	4.59	2.48	32.21
GIVEI	[6 13]	[6 13]	[6 11]	[8 15]

For the AL-SBAS system, both IGPs are used to calculate an augmented position, however, for EGNOS the IGPs at 25° range from 0 m to 63.875 m, which indicates that this IGP is not monitored, or it is marked Do Not Use. The GIVEI is an indicator of the vertical ionospheric error.

It can be noted that for some IGP points, EGNOS cannot calculate the ionospheric delay, due to the lack of RIMS in Algeria.

The implementation of a RIM in the country will permit further improvement of the corrections transmitted by the EGNOS system, particularly ionospheric correction [10].

To better analyze the impact of the reference station to modelling ionospheric error, a comparison of the temporal variation of ionospheric delay over 24 hours for IGP at 25° in latitude and 0° in longitude was performed. The variation of this correction is presented in the two Figures 10 and 11 for EGNOS and AL-SBAS.

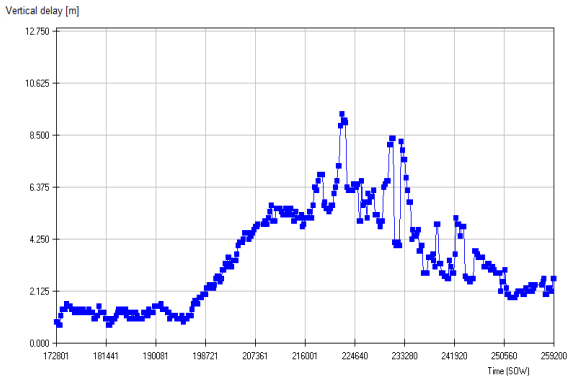

Figure 10. Variation of ionospheric delay over 24 hours for IGP (25° in latitude and 0° in longitude) using AL-SBAS

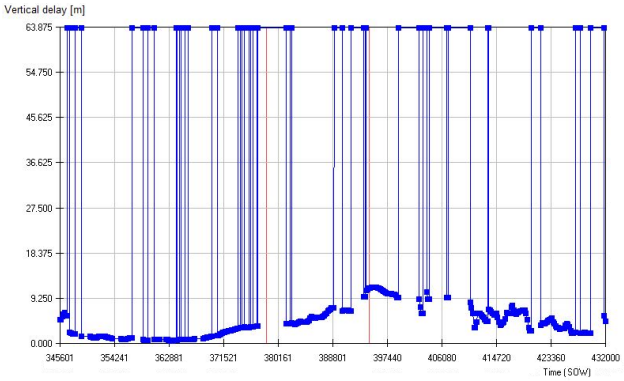

Figure 11. Variation of ionospheric delay over 24 hours for IGP (25° in latitude and 0° in longitude) using EGNOS

For latitude 25°, it is clear to see the lack of data, related to the "Not Monitored" state of EGNOS, while for AL-SBAS, this value varies between 1 m and 9 m.

IV. CONCLUSION

Algeria has been developing a satellite-based augmentation system called Algerian Satellite Based Augmentation System (AL-SBAS). The service area is limited to Algeria and nearby countries. The AL-SBAS augments the GPS standard positioning service by providing differential GPS corrections and integrity monitoring information.

The main objective of this work is to analyse and compare the corrections transmitted by AL-SBAS and EGNOS in Algeria. The major conclusions reached of the analysis performed are:

- The augmentation of AL-SBAS covers the entire country of Algeria, while the EGNOS system covers only the northern part of the country.
- Results of the AL-SBAS performance confirmed that ionospheric corrections from the currently available reference stations are more accurate than EGNOS, particularly in the southern part of Algeria.

These encouraging results open the possibility of a better application of the Algerian SBAS corrections in the future. In addition, it is recommended to test the availability and the effectiveness of AL-SBAS corrections by using a low cost receiver in real time.

As a perspective, we encourage the cooperation between the African air navigation services to accelerate the SBAS services deployment and provision to meet requirements of the aviation and extend the coverage of AL-SBAS system by adding reference stations in neighboring countries in order to improve the system performance.

REFERENCES

[1] B. Jin, S. Chen, D. Li, E. Takka, Z. Li and P. Qu, ''Ionospheric correlation analysis and spatial threat model for SBAS in China region'', Advances in Space Research, vol. 66, Issue 12, pp. 2873-2887, 2020.

[2] L. S. Lasisi, L. Dongjun and C. R. Chris, ''Nigcomsat-1R Satellite-Based Augmentation System (SBAS) Test Bed Trial: A Scientific Explanation'', Recent Developments in Engineering Research. vol. 11, pp. 75-85, 2021, https://doi.org/10.9734/bpi/rder/v11/734D.

[3] T. Authié, M. Dall'Orso, S. Trilles, H. Choi, H. Kim, J. Lee and G. Nam, ''Performances Monitoring and Analysis for KASS'', In Proceedings of the 30th International Technical Meeting of the Satellite Division of The Institute of Navigation (ION GNSS+ 2017), pp. 958-978, September, 2017.

[4] A. Euldji, ''SBAS system of Algeria'', RNSS Symposium, Abuja, Nigeria, October 5, 2018.

[5] J. Kozuba, K. Krasuski, J. Ćwiklak and H. Jafernik, ''Aircraft position determination in SBAS System in air transport'', In Proceedings of the 17th International Conference Engineering for rural development, Jelgava, Latvia, pp. 23-25. May, 2018.

[6] R. Li, S. Zheng, E.Wang, J. Chen, S. Feng, D. Wang. and L. Dai, ''Advances in BeiDou Navigation Satellite System (BDS) and satellite navigation augmentation technologies'', Satellite Navigation, vol.1, issue 1, pp. 1-23, 2020.

[7] National Coordination Office for Space-Based Positioning. L1 C/A PRN Code Assignments. edition. Washington D.C. (United States). Available at https://www.gps.gov/technical/prn-codes/L1-CA-PRN-code-assignments-2021-Jun.pdf. June 2021.

[8] H. Yoon, H. Seok, C. Lim and B. Park, ''An online SBAS service to improve drone navigation performance in high-elevation masked areas'', Sensors, vol. 20, issue 11, pp. 3047, 2020.

[9] CNES site: ftp://serenad-public.cnes.fr.

[10] W.Gurtner, ''RINEX: The Receiver Independent Exchange Format Version 2.11.UNAVCO'', https://www.ngs.noaa.gov/CORS/RINEX211.txt. 2007.

[11] L. Tabti, S. Kahlouche, B. Benadda and B.Beldjilali, ''Improvement of a single-frequency GPS positioning performance based on EGNOS corrections in Algeria'', Journal of Navigation, Cambridge. https://doi.org/10.1017/S037346331900095X. 2020.

[12] ESA. ''User Guide for EGNOS Application Developers'', ED 2.0. Luxembourg. European Commission, Available at: https://egnos-user-support.esspsas.eu/. 2011.

 ISBN: 978-1-68558-035-3

Review on Recent Trends and Applications of Vivaldi Antenna in the Range of 1 GHz – 40 GHz

Nitin Muchhal, Renato Zea Vintimilla, Yaarob Fares, Mostafa Elkhouly
Fraunhofer Institute for Integrated Circuits IIS, Am Wolfsmantel 33, 91058 Erlangen, Germany
{firstname.lastname@iis.fraunhofer.de}
*Corresponding author e-mail: nmuchhal@gmail.com

***Abstract*— This paper reviews several recently used methods to ameliorate the performance of Vivaldi antennas working in the vital frequency range of 1 - 40 GHz. In recent years, numerous researchers have suggested various methods to improve Vivaldi antenna's performance. Some of the techniques include the use of dielectric lens, metamaterial, Electromagnetic Band Gap, Corrugations, Slot, Parasitic patch between radiators, Substrate shape and choice of permittivity etc. Moreover, this paper reviews various major applications of Vivaldi antennas in recent times e.g., 5G/mmWave communication, Satellite communication (SATCOM), MIMO, UWB, Vehicular communication, etc.**

Keywords- Vivaldi antenna; 5G/mmWave; SATCOM; RADAR; UWB; MIMO; Wireless Communication.

I. INTRODUCTION

The need for an antenna with characteristics like wide bandwidth and high directivity has grown due to the enormous surge in broadcast and wireless communication technologies. Broadband antennas find use in various applications such as SATCOM, RADAR, remote sensing, microwave imaging, etc. A Vivaldi antenna is a type of Tapered Slot Antenna (TSA) that was first discovered and studied by Gibson in 1979 [1]. The conventional design of a TSA antenna is a tapered slot engraved on the metal over the dielectric substrate which is also an end-fire radiator. TSA has some models depending on the variations of the tapered-shaped slot. The most used are: Linear TSA (LTSA) [2], Constant TSA (CTSA) [3] and Exponentially TSA. Exponentially TSA design is also known as Vivaldi antenna. The Antipodal Vivaldi antenna, also known as the dual exponentially tapered slot antenna (DETSA) forms part of the end-fire tapered slot family of antennas Figure 1 is an illustrative representation of the generalized form of a Vivaldi antenna. By tapering the microstrip line, the feeding structure transition is accomplished [4].

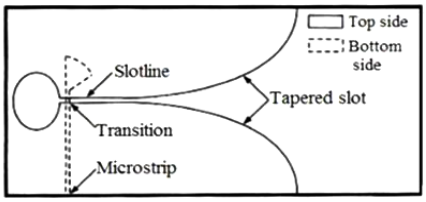

Figure 1. Structure of Vivaldi antenna [5].

The structure of this paper is as follows: A brief description of basic design and characteristics of Vivaldi antenna are given in Section I. Section II discusses various optimized Vivaldi antenna designs for various applications, e.g., (a) SATCOM/Radar/5G (b) UWB application (c) Wireless and Vehicular communication (d) Other miscellaneous applications. Finally, conclusions are given in Section III, followed by references.

II. VARIOUS APPLICATIONS OF VIVALDI ANTENNA

Vivaldi antennas are finding applications in all the major areas of communication systems. Some of them are listed as follows, along with their design methodology:

A. SATCOM/Radar/5G

Ullah et al. [6] proposed the design of an Antipodal Vivaldi Antenna (AVA) for 5G communication and Ku-band usages, as shown in Figure 2. The top layer of the design contains an array of eight elements having split-shaped leaf design fed by a power divider and the bottom layer contains truncated ground. Puskely et al. [7] proposed a dielectric loaded antipodal SIW Vivaldi antenna with high gain operating in the Ka band (25 - 40 GHz), as shown in Figure 2. An improved impedance matching with better directional radiation pattern is attained by the combination of dielectric loading, printed transition and corrugated ripples fabricated on the arms of antenna.

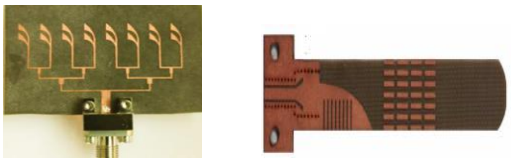

Figure 2. Fabricated prototypes [6][7].

Emre et al. [8] proposed a high gain UWB Vivaldi antenna array for Synthetic Aperture Radar (SAR) applications as shown in Figure 3. First, the Vivaldi antenna's single element is designed for ultra-wide band operation in the X-band and Ku-band frequency range. Subsequently, edge grooves are created on the sides of exponential etched patch surface in order to shield the proposed antenna from surface currents. Furthermore, the

 ISBN: 978-1-68558-035-3

parasitized element is complemented to increase the antenna gain. Kähkönen et al. [9] proposed an 18–30 GHz dual–polarized Vivaldi antenna array design for satellite communication as shown in Figure 3. The array consists of 4×4 dual-polarized antenna elements and RF module. The RF module comprises amplifiers and phase shifters to control the antenna elements. Zhang et al. [10] suggested a miniaturized, wide band dual-polarized Vivaldi antenna with reduced Radar Cross Section (RCS), as shown in Figure 3. Two single-polarized Vivaldi elements are arranged in a cross-shape to create the dual-polarized antenna with S11<-10 dB covering the spectrum from 1.8 to 6 GHz. The RCS of the antenna can be reduced over a wide frequency band by creating symmetric rectangular slots and curving metallic portion from the radiating surfaces.

Figure 3. Fabricated prototypes [8][9][10].

Dixit et al. [11] proposed a 1 × 4 AVA array for various 5G services as shown in Figure 4. The proposed antenna operates over 24 – 29 GHz and 30 – 40 GHz frequency ranges and possesses high gain. The size of antenna is miniaturized with help of corrugations which also improve front-to-back ratio augmenting the gain. To increase the bandwidth, optimized corporate feeding is used. Moosazadeh et al. [12] proposed an AVA antenna Surrounded by Dielectric (AVA-SD) with operating frequency, ranging from 5 to 40 GHz for mmWave imaging, radio astronomy, etc., as shown in Figure 4. The conventional AVA is enclosed by dielectric material (Teflon) to suppress higher-order modes and also to enhance antenna gain at higher frequency. The surrounding dielectric area is slightly expanded beyond the antenna to contain most of the energy. Kuriakose et al., [13] proposed a high gain UWB Vivaldi antenna for Through-Wall Radar (TWR) applications with operating frequency ranging from 1.8 GHz to 12 GHz, as shown in Figure 4. First, a broadband Vivaldi antenna is designed using exponentially tapered slot. Then, corrugations and periodic grating elements are introduced along the length of the antenna arm to enhance the gain.

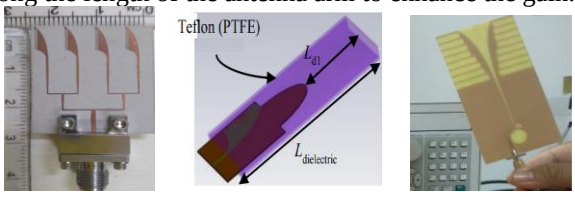

Figure 4. Fabricated prototypes [11][12][13].

Cheng et al. [14] proposed a small sized Vivaldi Antenna for Ground Penetrating Radar (GPR) system as shown in Figure 5. In the proposed design, a Side Lobe Suppressor (SSR) and Artificial Materials Lens (AML) are inserted to increase the gain and radiation capabilities of the GPR antenna. SSR mostly affects low-frequency EM waves, while AML primarily affects high-frequency EM waves. Ramanujam et al. [15] proposed the design of upgraded and compact AVA array for 28 GHz 5G millimeter wave (mm-wave) application with reduced coupling. The design as shown in Figure 5 consists of eight radiating elements with slots on the ground plane and the radiating arm to increase gain and reduce mutual coupling.

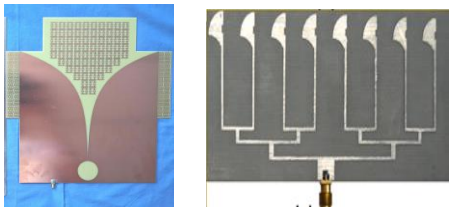

Figure 5. Fabricated prototypes [14][15].

Elabd et al. [16] proposed a broadband MIMO Vivaldi 5G base station antenna for frequency bands (28 GHz and 38 GHz) as shown in Figure 6. The proposed antenna consists of two orthogonally polarized antennas with better isolation using a novel EBG structure. Hence, the final design consists of a two-element beam switch MIMO Vivaldi antenna with electromagnetic band gap structure. Paul et al. [17] proposed a wide band (2 - 28 GHz) Vivaldi antenna, as shown in Figure 6, for satellite and 5G bands in Sub-6 GHz applications using optimization technique. To upgrade the performance, particularly the bandwidth and gain of the antenna, it includes ten corrugated side slots on radiating arm, two circular slots, and one via near feed point.

Figure 6. Fabricated prototypes [16][17].

Kumar et al. [18] proposed a wideband (15 - 40 GHz) AVA by integrating a V shaped Negative Index Metamaterial (NIM). The ‘V’-shaped MTM unit cells are positioned at the upper surface amidst two radiators in order to radiate a strong electric field in the end-fire direction.

B. Ultra-Wide Band (UWB) Applications

Yin et al. [19] projected a compact, wideband Vivaldi antenna comprising a half leaf-shape radiating arm with row of metallized vias making a HM-Vivaldi design, as shown in Figure 7. Further, when it is combined with truncated

ground plane, it improves the impedance matching of HM-Vivaldi and hence the bandwidth. An UWB ranging from 5.3 - 40 GHz with S11< -10 dB is accomplished. Wang et al. [20] proposed removal of the redundant substrate from the metallic flares of the proposed antenna and applying dual slotted edges, as shown in Figure 7, to enhance the radiation characteristics. Also, a microstrip-to-stripline transition is incorporated for better impedance matching. The design functions well over 10–40 GHz with S11 < -10dB providing good bandwidth and can be used for a wide range of applications for wireless communication. Li et al. [21] proposed an UWB metamaterial slab (meta-slab) loaded AVA with high gain and stable radiation pattern, as shown in Figure 7. The energy is transmitted to the end fire direction with help of the high permittivity meta-slab, which absorbs it from the tapered slot. Antenna S11 has a measured value of less than -10 dB between 3.6 and 40 GHz.

Figure 7. Fabricated prototypes [19][20][21].

Nassar et al. [22] proposed a unique method for enhancing the bandwidth and directivity of a wide band (2-32 GHz) antipodal Vivaldi antenna structure as shown in Figure 8. The technique is based on inserting a parasitic elliptical patch on the aperture to augment the field coupling amid the arms and create more radiation towards the end fire direction. Mazhar et al. [23] proposed a compact and wideband (5-40 GHz) circular Vivaldi antenna, as shown in Figure 8. The circular Vivaldi antenna is embedded with configuration of log periodic slots and achieves advantages of high gain and low side lobe levels at higher frequencies. Chen et al. [24] proposed a dual-band and dual-polarized nested Vivaldi antenna in frequency range 2 - 40 GHz. The proposed Vivaldi antenna comprises of a 2–8 GHz section along with a 8–40 GHz section nested together. These two nested Vivaldi antennas are arranged in a cross-shape to achieve the antenna's dual-polarized radiation.

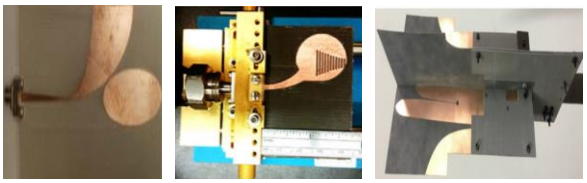

Figure 8. Fabricated prototypes [22][23][24].

Wan et al. [25] proposed design of ultra-wideband Vivaldi antenna with frequency band 3.3–40 GHz, as shown in Figure 9. A trapezoidal dielectric substrate is embedded in the direction of the major axis centred around conventional antipodal Vivaldi antenna, which enhances the directional radiation performance, e.g., high efficiency, low cross polarization ratio and high Front to Back Ratio (FBR). For UWB communications, Natrajan et al. [26] proposed an improved AVA with compact size and large bandwidth by adding another petal to conventional AVA as shown in Figure 9. Through this development, it increases the electrical length of the radiator and thereby reduces the lower operating frequency. Hence, adding another petal results in small size and increased bandwidth (2.4 - 20 GHz). Alhawari et al. [27] proposed a Multiple Input Multiple Output (MIMO) antenna on denim substrate exhibiting dual polarization and low mutual coupling with UWB bandwidth of 5–40 GHz. The antenna, as shown in Figure 9, is integrated with staircase meander line; thereafter, it is embedded with the metamaterial structure that reduces mutual coupling, increasing the gain and efficiency.

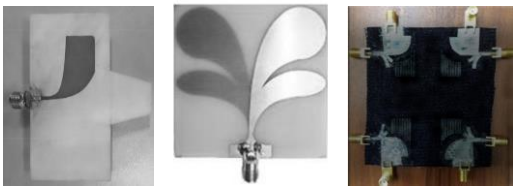

Figure 9. Fabricated prototypes [25][26][27].

Natarajan et al. [28] proposed a low cross-polarized and small sized antipodal Vivaldi antenna operating in the frequency range from 3.7 GHz to over 18 GHz as shown in Figure 10. The miniaturization in size is achieved by structurally modifying the radiating fins without changing the dimensions of antenna. Altering the fin's structure results in the diminution of lower operating frequency and hence the size is reduced. Zhang et al. [29] proposed a compact and wide-band Antipodal Vivaldi Antenna (AVA) for UWB applications, as shown in Figure 10. The radiator's conventional exponential tapering edge is substituted with an arc curve in the design to make the AVA more compact. In order to enhance its gain at high-frequency, the AVA is additionally equipped with a "director" and a "convex lens." The proposed antenna is compact with an operating frequency range from 3.01 to 10.6 GHz.

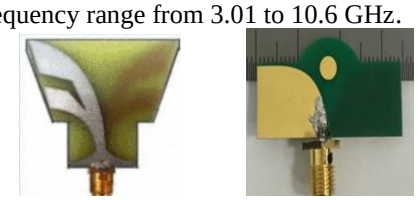

Figure 10. Fabricated prototypes [28][29].

C. Wireless and Vehicular Communication

For vehicular communications, a three-port diversity antenna generating three-directional radiation pattern was

proposed by Natarajan et al. [30]. It comprises of three Vivaldi antennas interconnected on a single PCB as shown in Figure 11. The second radiating wing is supplemented with the primary with twin line transition. It provides ultra-wideband features with end-fire radiation pattern and bandwidth ranging from 5 to 11 GHz. Jeon et al. [31] proposed a dual-polarized Vivaldi antenna for the Over-The-Air (OTA) testing and measurement of communication devices which are used in the frequency band of 3 – 7 GHz. By vertically interconnecting two planar Vivaldi antennas, the dual-polarization capability is achieved. For the broadband impedance matching of the antenna, a λ/4 long balun is used. Shan et al. [32] proposed a developed Vivaldi antenna with planar directors near the tapering slot's aperture and transverse slots are etched on the edges for vehicular wireless communication Systems. An antenna with planar directors and transverse slots is designed for IEEE 802.11a (4.9 – 5.93 GHz) vehicular communication, as shown in Figure 11.

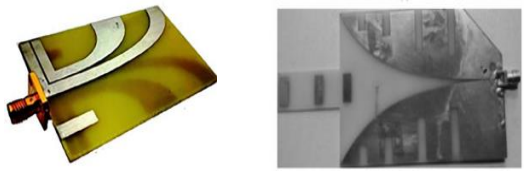

Figure 11. Fabricated prototypes [30][32].

For Vehicle-to-Vehicle (V2V) communication, a switching beam antenna system using four Vivaldi antennas is proposed by Ameen et al. [33], as shown in Figure 12. Vivaldi's operation is decided by switches which make particular antenna active. Tiwari et al. [34] proposed a slotted Vivaldi antenna for the wireless communication applications in the range of 3.5-8.4 GHz for WLAN, WiMAX and HiperLAN applications. Circular and triangular slots are etched on radiating arm of antenna for miniaturization and creating various frequency bands. Güneş et al. [35] proposed a tri-band AVA for WLAN and IoT applications. The antipodal Vivaldi antenna is made up of a Frequency Selective Surface (FSS) inspired director made up of an array of sub-wavelength rectangular patches and meander slotted lines etched on the edges of tapered metallic parts. FSS is used to reduce side lobe level. Bulgaroni et al. [36] proposed a novel design made by an array of two AVAs placed opposite to each other and fed via a microstrip to Coplanar Strip (CPS) transition, as shown in Figure 12. The feed in both antennas is out of phase. The proposed antenna shows four bands in frequency range of 1.85 - 6.9 GHz covering all important frequency bands for wireless technologies e.g, WLAN, Bluetooth, WiMAX, ISM band.

Figure 12. Fabricated prototypes [33][35][36].

Saleh et al. [37] proposed a non-uniform transmission line (NTL) based Vivaldi non-uniform slot profile antenna, as shown in Figure 13. Reduction in the taper slot length by 33% was achieved by this. The proposed antenna provides S11 < −10 dB through 2.4 –13.55 GHz and finds use in various wireless communication applications. Kapoor et al. [38] proposed a vehicular antenna, as shown in Figure 13, to cover the frequency bands for LTE and the mid-band fifth-generation (5G) systems by modifying the Vivaldi antenna which is in form of tapered slot structure. The antenna effectively connects mobile cellular networks and Internet on Vehicle (IoV) systems by virtue of its excellent directional radiation capability.

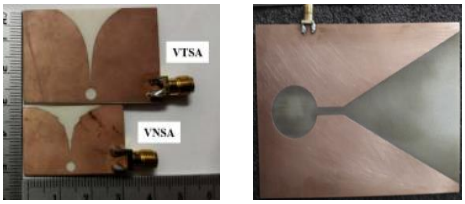

Figure 13. Fabricated prototypes [37][38].

D. Miscellaneous

Biswas et al. [39] proposed a compact and wide band fractal Vivaldi antenna by implementing the nature fern inspired fractal leaf structure, as shown in Figure 14. The impedance bandwidth of the proposed antenna is around 18.7 GHz ranging from 1.3 - 20 GHz. Zhang et al. [40] proposed the design of a novel Double-Slot Vivaldi Antenna (DSVA) with impedance bandwidth from 4.7 to 20 GHz, as shown in Figure 14. In comparison with former DSVAs, proposed antenna's radiation characteristics and gain finds great improvement by inserting the double-antipodal structure, director (lens) and corrugated edges in antenna aperture. Moosazadeh et al. [41] proposed an UWB AVA for civil engineering purposes. The inner edges of the upper and bottom radiators of the Conventional AVA (CAVA) have been suitably bent to enhance impedance bandwidth. Further, comb-shape slits have been applied to the edges of the radiators to improve F-to-B ratio and its gain. The result shows an impedance bandwidth between 1.65 - 18 GHz.

 ISBN: 978-1-68558-035-3

Figure 14. Fabricated prototypes [39][40][41].

Wang et al. [42] proposed a compact coplanar waveguide fed AVA embedded with two pairs of elliptically shaped loads and tapered slots for improving the radiation performance, as shown in Figure 15. The wide measured impedance band width achieved is from 1.3 GHz to 17 GHz. Moosazadeh et al. [43] proposed a modified UWB AVA for frequency range (3.4–40 GHz), as shown in Figure 15. The slit edge method is used to enhance the gain at lower frequencies, forming a Periodic Slit Edge AVA (PSEAVA). Thereafter, to further improve the directivity, a Trapezoid-shaped Dielectric Lens (TDL) is added as an addendum to the substrate. Moosazadeh et al. [44] proposed a compact AVA operating from 1 to 30 GHz for assessment of construction material. The conventional AVA's inner edges have been bent to extend the lower frequency range. Further, slit edge method is utilized to enhance the gain and lastly an elliptical-shaped dielectric lens is added to the substrate to attain high front-to-back ratio and gain.

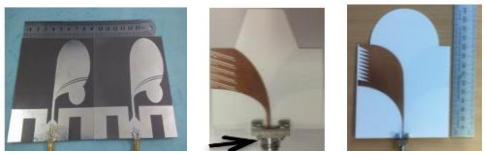

Figure 15. Fabricated prototypes [42][43][44].

Deng et al. [45] proposed an AVA integrated with Double-Ridged Substrate Integrated Waveguide (DRSIW), as shown in Figure 16. DRSIW can attain a lower cut-off frequency as compared to usual SIW due to the inserted ridge. Therefore, DRSIW-fed AVA achieves a decrease in cut-off frequency with improved bandwidth as compared to Vivaldi antennas fed by SIW. The bandwidth with $|S11| \leq -10$ dB lies in the range of 11.0 GHz to 40 GHz. Recently, [46] has proposed Vivaldi antenna array using Ceramic LTCC substrate materials for low loss, high frequency circuit carriers for 6G wireless communication technology and millimeter wave radar.

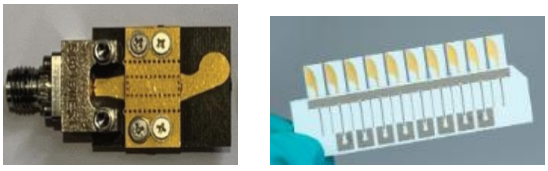

Figure 16. Fabricated prototypes [45] [46].

Vivaldi antenna has several advantages e.g., broadband characteristics, easy impedance matching to the feeding line, compact size, etc. In spite of many advantages of the Vivaldi antenna, it still suffers from a few drawbacks, such as tilted beam, moderate gain and mostly being costlier due to the complex fabrication process.

III. CONCLUSION

In this paper, various techniques for improving the performance of Vivaldi antenna along with their application areas are presented. The basic ideas behind the working principle of Vivaldi and various optimizing techniques are discussed. Further, several recent works using Vivaldi antenna for various areas of communication e.g., Satellite communication, Vehicular communication, Wireless application, RADAR, UWB, MIMO etc. are briefly reviewed.

ACKNOWLEDGEMENT

This work was carried out during the tenure of an ‘ERCIM (The European Research Consortium for Informatics and Mathematics) Alain Bensoussan Fellowship’ programme Founded in 1988.

REFERENCES

[1] P.J. Gibson, “The Vivaldi Aerial”, IEEE 9th European Microwave Conference, 1979 - Brighton, UK, pp. 101–105.

[2] R. Janaswamy and D. Schaubert, "Analysis of the tapered slot antenna," in IEEE Transactions on Antennas and Propagation, vol. 35, no. 9, pp. 1058-1065, September 1987.

[3] Y. J. Chen, Z. Xu, Y. Yuan and D. Sun, "Step-constant Tapered Slot Antenna with multiple bandwidths in millimetre-wave application," IET Intl. Radar Conference, 2009, Guilin, pp. 1-3.

[4] H. Azodi, X. Zhuge and A. Yarovoy, "Balanced antipodal Vivaldi antenna with novel transition from feeding line to the flares," Proceedings of the 5th European Conference on Antennas and Propagation (EUCAP), 2011, pp. 1279-1283.

[5] J. Shan, A. Xu and J. Lin, "A parametric study of microstrip-fed Vivaldi antenna," IEEE International Conference on Computer Communications (ICCC), Chengdu, 2017, pp. 1099-1103.

[6] R. Ullah, F. Faisal, D. Choi, and B. Kamal, “High-Gain Vivaldi Antenna with Wide Bandwidth Characteristics for 5G and Ku-Band Radar Applications”, Electronics. 2021; 10(6):667.

[7] J. Puskely, J. Lacik, Z. Raida and H. Arthaber, "High-Gain Dielectric-Loaded Vivaldi Antenna for Ka Band Applications," IEEE Antennas Wireless Prop. Letters, vol.15, pp. 2004-2007, 2016.

[8] H. Emre and A. M. Emre, “High Gain Ultrawide Band Vivaldi Antenna Design for Mini/Micro Satellite Synthetic Aperture Radar Applications” IEEE 2019 9th International Conference on Recent Advances in Space Technologies (RAST), Istanbul, pp. 491-495, 2019.

 ISBN: 978-1-68558-035-3

[9] H. Kähkönen, J. A.-Laurinaho and V. Viikari, "A Modular Dual-Polarized Ka-Band Vivaldi Antenna Array," in IEEE Access, vol. 10, pp. 36362-36372, 2022.

[10] K. Zhang et al., "Compact Ultra wideband Dual-Polarized Vivaldi Antenna with Radar Cross Section Reduction,"IEEE Antennas Wireless Prop. Letters, vol.21, no.7, pp.1323-1327, 2022.

[11] A. S Dixit, S. Kumar, S. Urooj, and S. A. Malibari, "A Highly Compact Antipodal Vivaldi Antenna Array for 5G Millimeter Wave Applications", Sensors, vol. 21, 2360, 2021.

[12] M. Moosazadeh, "High-Gain Antipodal Vivaldi Antenna Surrounded by Dielectric for Wideband Applications" IEEE Transactions on Antennas Prop., vol. 66(8), pp. 4349-4352, 2018.

[13] T. A Kuriakose and A. S George, "Improved High Gain Vivaldi Antenna Design for Through-wall Radar Applications," 2020 IEEE International Symposium on Antennas & Propagation (APSYM), 2020, Cochin, pp. 58-61.

[14] H. Cheng, H. Yang, Y. Li and Y. Chen, "A Compact Vivaldi Antenna with Artificial Material Lens and Sidelobe Suppressor for GPR Applications," IEEE Access, vol. 8, pp. 64056-64063, 2020.

[15] P. Ramanujam, M. Ponnusamy, and K. Ramanujam, "A compact wide-bandwidth Antipodal Vivaldi Antenna array with suppressed mutual coupling for 5G mm-wave applications", AEU – Intl. Journal of Electronics and Communications, vol. 133, 2021.

[16] R. H. Elabd, H. H. Abdullah and M. Abdelazim, "Compact Highly Directive MIMO Vivaldi Antenna for 5G Millimeter-Wave Base Station", Journal of Infrared, Millimeter, and Terahertz Waves, vol. 42, pp. 173–194 , 2021.

[17] L. C. Paul and Md. M. Islam, "A Super Wideband Directional Compact Vivaldi Antenna for Lower 5G and Satellite Applications", vol. 2021 | Article ID 8933103.

[18] S. Kumar and A.S. Dixit, "Wideband Antipodal Vivaldi Antenna Using Metamaterial for Micrometer and Millimeter Wave Applications", J Infrared Milli Terahz Waves 42, pp. 974–985, 2021.

[19] Z. Yin, G. He, X. -X. Yang and S. Gao, "Miniaturized Ultra wideband Half-Mode Vivaldi Antenna Based on Mirror Image Theory," IEEE Antennas and Wireless Prop Letters, vol. 19, no. 4, pp. 695-699, April 2020.

[20] N. Wang, M. Fang, H. T. Chou, J.R. Qi and L.Y. Xiao, "Balanced Antipodal Vivaldi Antenna with Asymmetric Substrate Cut-out and Dual-Scale Slotted Edges for Ultra wide band Operation at Millimeter-Wave Frequencies," IEEE Transactions on Antennas Propagation, vol. 66, no. 7, pp. 3724-3729, July 2018.

[21] X. Li, H. Zhou, Z. Gao, H. Wang and G. Lv, "Metamaterial slabs covered UWB antipodal Vivaldi antenna", IEEE Antennas and Wireless Prop. Letters 16, pp. 2943–2946, 2017.

[22] T. Nassar and T. M. Weller, "A Novel Method for Improving Antipodal Vivaldi Antenna Performance," in IEEE Transactions on Antennas and Propagation, vol. 63, no. 7, pp. 3321-3324, 2015.

[23] M. Waqas, K. David, Q. Aqeel, "Log periodic slot-loaded circular vivaldi antenna for 5-40 GHz UWB applications", Microwave and Optical Technology Letters, 59(1), pp. 159-163, 2017.

[24] D. Chen et al., "2–40 GHz dual-band dual-polarised nested Vivaldi antenna", IET Microwaves, Antennas & Propagation, vol. 13, issue 2, pp. 163-170, 2019.

[25] F. Wan, J. Chen and B. Li, "A novel ultra-wideband antipodal Vivaldi antenna with trapezoidal dielectric substrate", Microwave and Optical Technology Letters 60, pp. 449–455, 2018.

[26] R. Natarajan et al**.,** **"**Modified antipodal Vivaldi antenna for ultra-wideband communications", IET Microwaves, Antennas & Propagation, vol. 10, issue 4, pp. 401-405, 2016.

[27] R.H. Alhawari et al., "Wearable Metamaterial Dual-Polarized High Isolation UWB MIMO Vivaldi Antenna for 5G and Satellite Communications", *Micromachines*, 12(12):1559, 2021.

[28] R. Natarajan, J. V. George, M. Kanagasabai and A. Kumar Shrivastav, "A Compact Antipodal Vivaldi Antenna for UWB Applications," in IEEE Antennas and Wireless Propagation Letters, vol. 14, pp. 1557-1560, 2015.

[29] X. Zhang, Y. Chen, M. Tian, Liu J, and H. Liu, "A compact wideband antipodal Vivaldi antenna design" International Journal of RF and Microwave Computer-Aided Engineering, vol. 29, issue 4, April 2019.

[30] R. Natarajan, G. N. Alsath, M. Kanagasabai, S. Bilvam and S. Meiyalagan, "Integrated Vivaldi antenna for UWB/diversity applications in vehicular environment", International Journal of RF and Microwave Computer-Aided Engineering 30, pp. 1–10, 2020.

[31] G.-H. Jeon, P. A. Dzagbletey, and J.-Y. Chung, "A Cross-Joint Vivaldi Antenna Pair for Dual-Pol and Broadband Testing Capabilities", Journal of Electromagnetic Engineering and Science, vol. 21, no. 3, 201-209, Jul. 2021.

[32] H. He, W. Shan, C. Fan, Z. C. Mo, F. H. Yang and J. H. Chen, "An Improved Vivaldi Antenna for Vehicular Wireless Communication Systems," in IEEE Antennas and Wireless Propagation Letters, vol. 13, pp. 1505-1508, 2015.

[33] M. Allam, I. A Mohamed, H. Elsadek, and W. R Anis, "Switched Beam Antenna System for V2V Communication in 5G Applications", Applied Computational Electromagnetics Society Journal (ACES), pp. 1438-1444, vol. 36, no. 11, Nov. 2021.

[34] S. Tiwari, T. Ghosh and J. Sahay, "Miniaturization of Vivaldi antenna for different wireless communication applications," 2018 4th International Conference on Recent Advances in Information Technology (RAIT), 2018, pp. 1-6, Dhanbad, India.

[35] F. Güneş, İ.Ö Evranos, and M.A. Belen, "A compact triband antipodal Vivaldi antenna with frequency selective surface inspired director for IoT/WLAN applications", Wireless Netw 27, pp. 3195–3205, 2021.

[36] R. Bulgaroni, W. M. Torres, and H. X. Araujo, "Low-cost quad-band dual antipodal Vivaldi antenna using microstrip to CPS transition", pp. 2315-2320, vol. 60, issue 9, September 2018.

[37] S. Saleh, W. Ismail, I. S. Z. Abidin, M. H. Jamaluddin, M. H. Bataineh and A. S. Al-Zoubi, "Novel Compact UWB Vivaldi Non-uniform Slot Antenna with Enhanced Bandwidth," in IEEE Transactions on Antennas and Propagation, vol. 70, no. 8, pp. 6592-6603, Aug. 2022.

[38] A. Kapoor, P. Kumar, and R. Mishra, "High gain modified Vivaldi vehicular antenna for IoV communications in 5G network", Heliyon (ScienceDirect), vol. 8, issue 5, 2022.

 ISBN: 978-1-68558-035-3

[39] B. Biswas, R. Ghatak and D. R. Poddar, "A compact Fern Fractal Leaf Inspired Wideband Antipodal Vivaldi Antenna for Microwave Imaging System," in IEEE Transactions on Antennas and Propagation, vol. 65, no. 11, pp. 6126-6129, Nov. 2017.

[40] Y. Zhang, E. Li, C. Wang and G. Guo, "Radiation Enhanced Vivaldi Antenna with Double-Antipodal Structure," in IEEE Antennas and Wireless Propag. Letters, vol. 16, pp. 561-564, 2017.

[41] M. Moosazadeh, S. Kharkovsky, J. T. Case and B. Samali, “Antipodal Vivaldi antenna with improved radiation characteristics for civil engineering applications”, IET Microwaves, Antennas & Propagation 11, pp. 796–803, 2017.

[42] Z. Wang, Y. Yin, J. Wu and R. Lian, "A Miniaturized CPW-Fed Antipodal Vivaldi Antenna with Enhanced Radiation Performance for Wideband Applications," in IEEE Antennas and Wireless Propagation Letters, vol. 15, pp. 16-19, 2016.

[43] M. Moosazadeh, K. Sergey, and T. Joseph.,” Microwave and millimetre wave Antipodal Vivaldi Antenna with trapezoid-shaped dielectric lens for imaging of construction material”, IET Microwave Antennas & Propn, vol. 10, issue 3, pp. 301-309, 2016.

[44] M. Moosazadeh, S. Kharkovsky, J. T. Case and B. Samali, "Miniaturized UWB Antipodal Vivaldi Antenna and Its Application for Detection of Void Inside Concrete Specimens," IEEE Antennas and Wireless Propagation Letters, vol. 16, pp. 1317-1320, 2017.

[45] J. -Y. Deng, R. Cao, D. Sun, Y. Zhang and L. -X. Guo, "Bandwidth Enhancement of an Antipodal Vivaldi Antenna Facilitated by Double-Ridged Substrate-Integrated Waveguide," in IEEE Transactions on Antennas and Propagation, vol. 68, no. 12, pp. 8192-8196, Dec. 2020.

[46] K. Reinhardt, M. Ihle, and P. Gierth, “Printed electronics for highest frequencies: 6 G wireless communication technology and mm wave radar”, 2022, Available: https://www.ikts.fraunhofer.de/en/blog/printed-electronics-for-highest-frequencies--6G-wireless-communication-technology-and-millimeter-wave-radar.html [last accessed April, 2023].

 ISBN: 978-1-68558-035-3

Design of High Gain Corrugated Antipodal Vivaldi Antenna With ∏ Shaped Metamaterial for SATCOM Applications

Nitin Muchhal*, Mostafa Elkhouly, Yaarob Fares, Renato Zea Vintimilla
Fraunhofer Institute for Integrated Circuits IIS, Am Wolfsmantel 33, 91058 Erlangen, Germany
{firstname.lastname@iis.fraunhofer.de}
*Corresponding author e-mail: nmuchhal@gmail.com

***Abstract*— A wideband and high gain corrugated epsilon negative index metamaterial (ENG) Antipodal Vivaldi Antenna (AVA) with gain>12 dBi and working in frequency range from 10 GHz - 25 GHz (for SATCOM applications) is proposed in this paper. The overall performance of the proposed AVA is enriched by using a triangular shaped corrugation slots and pi (∏) shaped epsilon negative metamaterial cells. The '∏' shaped metamaterial unit cells are positioned on the upper surface amid both radiators of AVA to emanate the intense electric field in the end-fire direction. The proposed antenna size is 22.6 mm × 15.8 mm x 1.6 mm and it is designed on the FR4 substrate. The maximum gain of the antenna is 12.2 dBi at 14.5 GHz.**

Keywords- Metamaterial; Corrugation; Antipodal Vivaldi Antenna (AVA); Gain; SATCOM.

I. INTRODUCTION

To accomplish pervasive connectivity on the globe, SATellite COMmunication (SATCOM) is a crucial constituent of next-generation wireless communications. In recent times, a significant amount of research work has been proposed to design various vital components [1][2] for SATCOM applications. The Vivaldi antenna was proposed and designed by Gibson for high-frequency applications [3]. Later, Gazit improved it by giving it an antipodal shape to enhance the bandwidth and gain [4]. By incorporating numerous enhancement methods e.g., adding parasitic patch, dielectric lens, array and metamaterial, the parameters of the Antipodal Vivaldi Antenna (e.g., directivity, bandwidth, reduction inside lobe level etc.) can be improved. In [5], a parasitic patch of elliptical shape is used to increase the directivity of the Antipodal Vivaldi Antenna (AVA), but it has the drawback of bigger size. The dielectric lens used in [6] upsurges the end-fire radiations, but at the cost of a large size. The AVA Array design proposed by [7] increases the gain but suffers from augmented mutual coupling due to proximity of antenna elements. Amongst several techniques, the enhancement technique using metamaterial is quite effective without increasing the size of an antenna. After an intensive literature review, it is established that little work is done on AVA with metamaterial for SATCOM applications. This paper presents a compact and enhanced gain AVA with '∏'(pi) shaped metamaterial for SATCOM applications.

The rest of the paper is structured as follows. Section II elaborates on the design of the proposed conventional AVA. Section III deals with the design of the corrugated AVA. Section IV covers the design and analysis of corrugated AVA with the novel metamaterial unit cells. The simulated results of the proposed AVA are discussed in Section V. The outcomes of the proposed AVA are concluded in Section VI, followed by references.

II. DESIGN OF CONVENTIONAL AVA (CAVA)

Antipodal Vivaldi Antenna (AVA) was first proposed by Gazit in 1988. It unveils superior features such as wideband, high gain, stable radiation pattern and easy fabrication and hence it can efficiently gratify the various requirements of SATCOM. It consists of tapered or exponential metallic patches on top and bottom plane with a microstrip feed line matching with the connector, as shown in Figure 1.

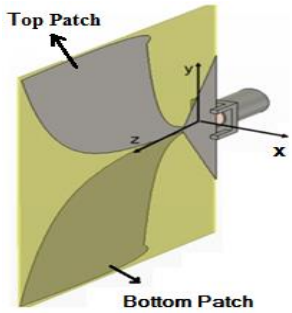

Figure 1. Antipodal Vivaldi Antenna [8]

Figure 2 depicts the geometry of the Conventional Antipodal Vivaldi Antenna (CAVA) simulated in HFSS ver. 13. This antenna consists of two parts: elliptical curved radiation flares and feed line. The top and bottom patches act as radiator and ground respectively. The antenna is designed on standard and economical substrate FR4 with a dielectric constant of 4.4, tan δ as 0.02 and thickness 1.6 mm and simulated using HFSS ver. 13. As the Antipodal antennas operate as a resonant antenna at the lower end of frequency band, the antenna length L1 and width W1 is determined based on the lowest frequency f_L, relative dielectric constant ε_r. The antenna dimensions are calculated by using the following equations [8]:

 ISBN: 978-1-68558-035-3

$$L_1 = \frac{c}{f_L}\sqrt{\frac{2}{\varepsilon_r + 1}} \quad (1)$$

$$W_1 = \frac{c}{2 f_L \sqrt{\varepsilon_r}} \quad (2)$$

The curve equations are given as

$$Y = \pm(R_1 e^{rx} + R_2) \quad (3)$$

Where R1 and R2 are given by:

$$R_1 = \frac{y_2 - y_1}{e^{rx2} - e^{rx1}} \quad (4)$$

$$R_2 = \frac{e^{rx2} y_1 - e^{rx1} y_2}{e^{rx2} - e^{rx1}} \quad (5)$$

Here, R1 and R2 are constants, ‘r’ symbolizes the increase rate of an exponential curve and, x1, y1, are the initial points and x2, y2 are the termination points of the exponential curve.

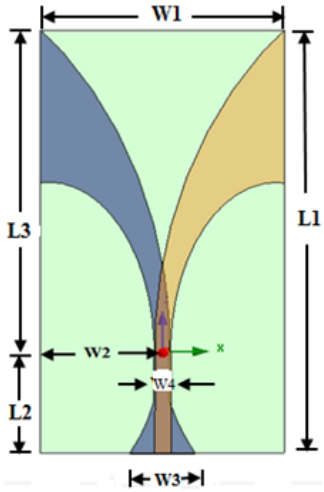

Figure 2. Structure of CAVA

The dimensions of the CAVA are calculated to have an optimized response over the desired bandwidth and they are found to be as follows: L1= 22.60 mm, L2 = 5.50 mm, L3= 17.1 mm, W1= 15.8 mm, W2= 7.2 mm, W3= 4.2 mm. The width of the microstrip feedline (W4) is calculated to match the characteristic impedance of 50 ohm which comes out to be W4= 1.25 mm. The radiating structure of the antenna is formed from the intersection of quarters of two ellipses, as explained in [9].

Figure 3 depicts the S11 response for the CAVA. From the curve, it can be seen that the designed CAVA resonates below -10 dB in the range of 10.8 GHz to more than 25 GHz. Figure 4 shows that CAVA achieves low gain at lower frequencies with maximum gain of 5.8 dBi only.

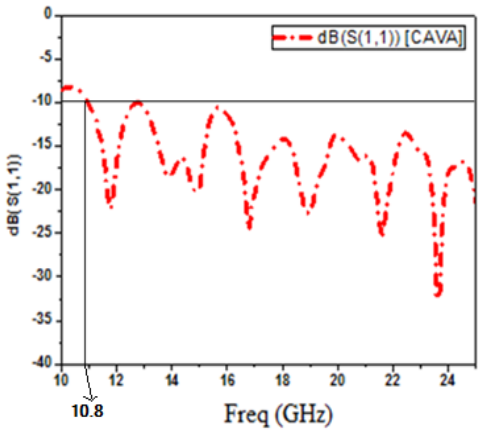

Figure 3. Frequency response of CAVA

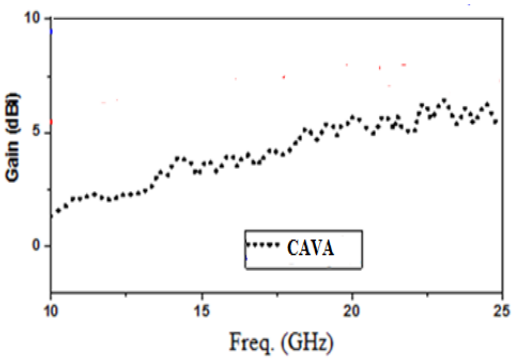

Figure 4. Gain plot of CAVA

Since the proposed CAVA dispenses low gain at lower frequencies, corrugation can be used to overcome this problem [10]. This will be explained in detail in Section III.

III. DESIGN OF CORRUGATED AVA

The low frequency performance of an AVA flare is enriched by the corrugation on its outer edges. Figure 5 depicts the design of the equilateral triangular corrugated AVA with slot side length, S = 0.85 mm.

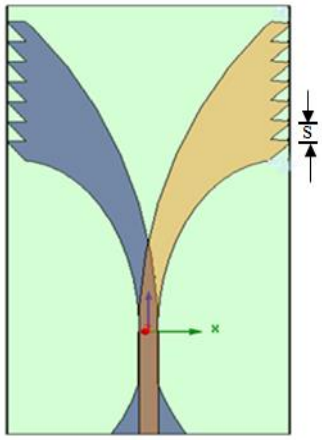

Figure 5. Structure of Corrugated AVA

 ISBN: 978-1-68558-035-3

The simulated S11 response of corrugated AVA is depicted in Figure 10. It can be seen that by adding corrugation, the lower cutoff frequency shifts to 10.3 GHz. The reason behind this shift in frequency is that the slot corrugation facilitates the electrical length of the inner taper profile to be elongated thereby extending the lower end cut-off frequency [11]. Further, the corrugation acts as a high impedance region due to which the maximum surface current remains towards the inner edge of the tapered slot reducing side and backlobe radiation, increasing the gain in boresight direction [12].

To further enhance the gain and improve the radiation characteristics, an array of metamaterial is commonly used on AVA aperture [13]. This will be explained in detail in Section IV.

IV. DESIGN AND ANALYSIS OF CORRUGATED AVA WITH METAMATERIAL (MTM)

To enhance the gain and characteristics of the proposed Vivaldi antenna, an array of epsilon negative metamaterial (ENG) unit cells is supplemented at its aperture. The proposed 'pi shape (π)' metamaterial is shown in Figure 6. The proposed MTM is placed inside a waveguide with Perfect Magnetic Conductors (PMC) on its top and bottom, Perfect Electric Conductors (PEC) on its side walls and two waveguide ports for excitation, as shown in Figure 7. Standard retrieving procedure is followed by using transmission and reflection coefficient of the unit cell, as described in [14], and it is found that the proposed metamaterial unit cell exhibits epsilon negative property, as shown in Figure 8. The optimized dimensions (in mm) of unit cell are as follows: A = 1.6, B= 0.25, C=1.35, D = 0.70

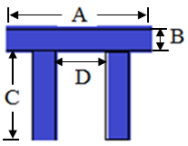

Figure 6 π shape Metamaterial Unit Cell

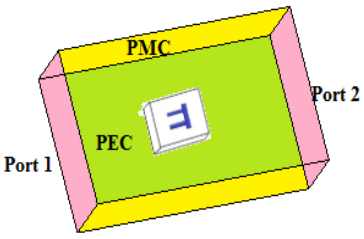

Figure 7. Simulation model of the proposed unit cell

Figure 8 illustrates the ENG behaviour of the unit cell with negative relative permittivity property in range of 14 GHz - 18 GHz.

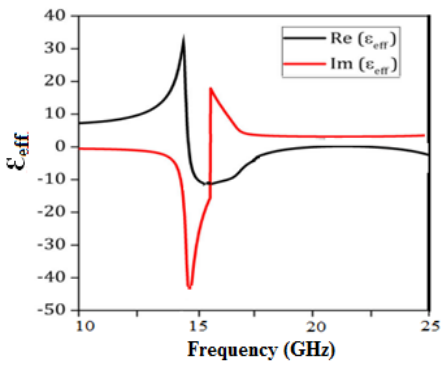

Figure 8. Permittivity graph of ENG unit cell

The MTM array was supplemented to the upper side of the antenna radiating aperture to augment the performance of the corrugated AVA. Using [15] and analysing by various placements and numbers of the proposed metamaterial cells for the desired frequency range, it was found that the proposed design with six MTM cells at 3-2-1 arrangement (from the top), as shown in Figure 9, attains the preferred bandwidth with better gain radiating maximum energy in the end-fire direction, as will be discussed in Section V.

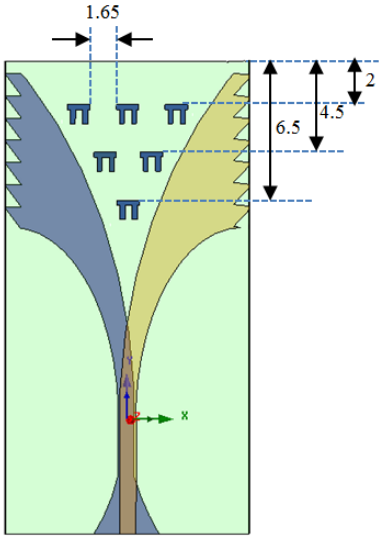

Figure 9. Corrugated AVA with Metamaterial (MTM) unit cells

V. RESULTS AND DISCUSSION

Figure 10 illustrates the simulated results of reflection coefficient (S11) with frequency for the corrugated AVA and corrugated MTM AVA. As can be noticed from the figure, the reflection coefficient of the corrugated AVA is below -10 dB for the frequency range of 10.3 GHz to 25 GHz. Applying the corrugation technique resulted in extension of the lower end frequency limit due to elongation of inner taper length. The negative index metamaterial

 ISBN: 978-1-68558-035-3

further ameliorated the lower cut-off frequency making S11<-10 dB for the entire range from 10 GHz - 25 GHz.

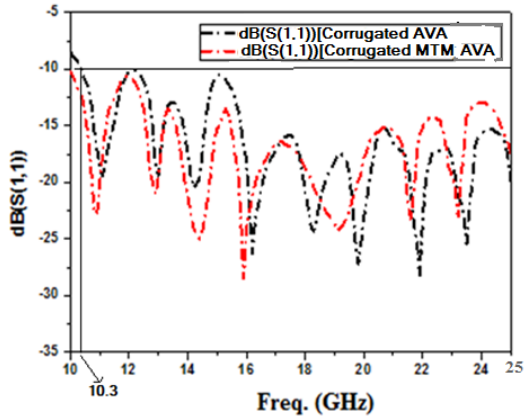

Figure 10. Comparison of Frequency response of Corrugated AVA and Corrugated MTM AVA

Figure 11 depicts the comparison of the gain plot of Corrugated AVA and Corrugated MTM AVA. The Corrugated AVA provides gain in the range of 6.5 dBi - 8.6 dBi, whereas the AVA-M provides the gain in the range of 7.3 dBi – 12.2 dBi with maximum gain achieved at 14.5 GHz. As evident from the gain plot, by integrating corrugation on both side edges of conducting arms, the gain of the proposed antenna increased significantly, especially at the lower end of the operating frequency band. Further, by integrating the metamaterial unit cells structure, the gain enrichment is more pronounced in the mid frequency band. Hence, the peak gain is enhanced by approximately 3.8 dBi in the desired range after inclusion of metamaterial unit cells, which is a significant gain enhancement without changing the antenna size.

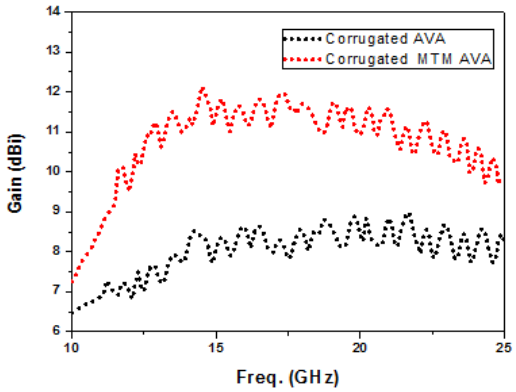

Figure 11. Comparison of Gain of Corrugated AVA and Corrugated MTM AVA

Figure 12 and Figure 13 illustrate the radiation patterns of the corrugated AVA and the proposed MTM antenna on the E-plane and H-plane at 10, 15 and 25 GHz, respectively.

It can be seen from the radiation pattern that loaded MTMs result in better directivity with improvement in gain [16] and possess enhanced radiation performance by suppressing the undesired side lobes [17] resulting in low side lobe levels.

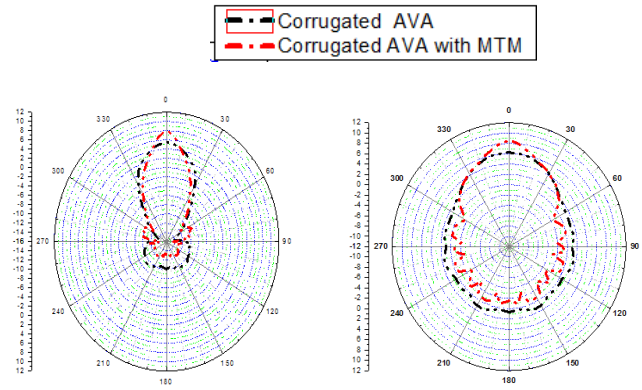

E Plane at 10 GHz

H Plane at 10 GHz

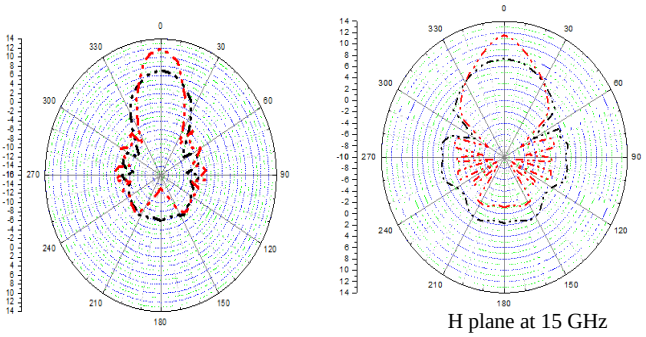

E plane at 15 GHz

H plane at 15 GHz

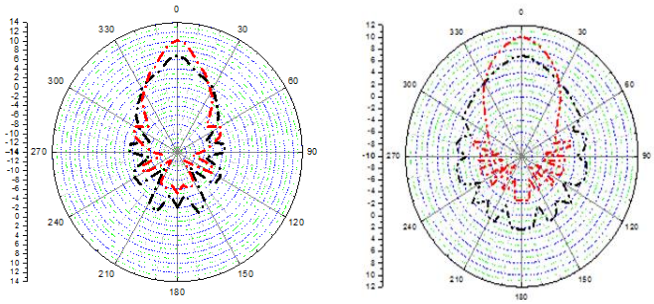

E Plane at 25 GHz

H Plane at 25 GHz

Figure 12. E plane radiation patterns

Figure 13. H plane radiation patterns

As it is evident that the proposed antenna offers higher directivity, but it can be costlier due to the complex fabrication process.

 ISBN: 978-1-68558-035-3

VI. CONCLUSION

This paper proposes the design and analysis of a high gain corrugated AVA with novel epsilon negative (ENG) metamaterial. The ENG metamaterial enhances the reflection coefficient with a wider bandwidth from 10 to 25 GHz without increasing the size. Further, the proposed corrugated MTM AVA enhances the gain by approximately 3.8 dBi as compared to corrugated AVA in the desired frequency range. As the proposed AVA design provides enhanced gain, improved return loss and compactness, it can be considered as a suitable candidate for satellite transmitter applications.

ACKNOWLEDGMENT

This work was undertaken during the tenure of an “ERCIM (The European Research Consortium for Informatics and Mathematics) Alain Bensoussan Fellowship” programme. Founded in 1988, ERCIM has members from leading European information technology and mathematics research establishments from 18 countries, with its head office in France.

REFERENCES

[1] K. -X. Li, Z. -J. Guo and Z. -C. Hao, "A Multipolarized Planar Phased Array for LEO SATCOM Applications," in IEEE Antennas and Wireless Propagation Letters, vol. 21, no. 11, pp. 2273-2277, Nov. 2022.

[2] N. Muchhal, M. Elkhouly, K. Blau and S. Srivastava, “Design of Highly Selective Band-pass Filter with Wide Stop-band using Open Stubs and Spurlines for Satellite Communication (SATCOM) Applications”, The Fourteenth International Conference on Advances in Satellite and Space Communications, SPACOMM 2022, April 2022, Barcelona, Spain.

[3] P. J. Gibson, "The Vivaldi Aerial," 1979 9th European Microwave Conference, 1979, pp. 101-105.

[4] E. Gazit,” Improved design of the Vivaldi antenna”, IEE Proceedings H-Microwaves, Antennas and Propagation, vol. 135(2), pp. 89–92, 1988.

[5] I. T. Nassar and T. M. Weller., “A novel method for improving antipodal Vivaldi antenna performance”, IEEE Transactions on Antennas and Propagation, 63(7), pp. 3321–3324, 2015.

[6] M. Moosazadeh, S. Kharkovsky, and J. T Case, “Microwave and millimetre wave antipodal Vivaldi antenna with trapezoid-shaped dielectric lens for imaging of construction materials”, IET Microwaves, Antennas & Propagation, 10(3), pp. 1–9, 2015.

[7] A. S. Dixit and S. Kumar, “A miniaturized antipodal vivaldi antenna for 5G communication applications” 7th international conference on signal processing and integrated networks (SPIN), pp. 800-803, 2020.

[8] S. Wang, X. D. Chen and C. G. Parini, "Analysis of Ultra Wideband Antipodal Vivaldi Antenna Design," 2007 Loughborough Antennas and Propagation Conference, Loughborough, UK, 2007, pp. 129-132.

[9] A. M. Abbosh, H. K. Kan, and M.E Bialkowski, “Design of compact directive ultra-wideband antipodal antenna”, Microwave and Optical Technology Letters, pp. 2448-2450, vol. 48, issue 12, Dec. 2006.

[10] A. S. Dixit and S. Kumar, "A Survey of Performance Enhancement Techniques of Antipodal Vivaldi Antenna," in IEEE Access, vol. 8, pp. 45774-45796, 2020.

[11] J. Bai, S. Shi, and D.W. Prather, “Modified compact antipodal Vivaldi antenna for 4–50 GHz UWB application”. IEEE Trans. Microw. Theory Tech. 59(4), pp. 1051–1057, 2011.

[12] Gaurav Kumar Pandey, Manoj Kumar Meshram, “A printed high gain UWB vivaldi antenna design using tapered corrugation and grating elements”, International Journal of RF and Microwave Computer-Aided Engineering, pp. 610-618, vol. 25 (7), September 2015.

[13] A. S. Dixit and S. Kumar, “The enhanced gain and cost-effective antipodal Vivaldi antenna for 5G communication applications”, Microwave and Optical Technology Letters, pp. 2365-2374, vol. 62 (6), 2020.

[14] N. Muchhal, S. Srivastava, and M. Elkhouly, "Analysis and Design of Miniaturized Substrate Integrated Waveguide CSRR Bandpass Filters for Wireless Communication", in Recent Microwave Technologies. London, United Kingdom: IntechOpen, 2022.

[15] M. Guo, R. Qian, Q. Zhang, L. Guo, Z. Yang, and Z.Wang, “High-gain antipodal Vivaldi antenna with metamaterial covers”, IET Microwaves, Antennas & Propagation , p. 2654-2660, vol. 13, issue 15, 2019.

[16] L Chen, Z Lei, R Yang, J Fan, X Shi. “A broadband artificial material for gain enhancement of antipodal tapered slot antenna”, IEEE Trans. Antennas Propag. 63(1): pp. 395-400, 2015.

[17] M. C. Johnson, S. L. Brunton, N. B. Kundtz and J. N. Kutz, "Sidelobe Canceling for Reconfigurable Holographic Metamaterial Antenna," in IEEE Transactions on Antennas and Propagation, vol. 63, no. 4, pp. 1881-1886, April 2015.

 ISBN: 978-1-68558-035-3